Chair of Astronautics
Prof. Prof. h.c. Dr. Dr. h.c.
Ulrich Walter

Term Paper

Correlation of the MOVE-II Digital Twin with In-Orbit Telemetry

RT-SA 2022-01

Author:
Johannes Koch

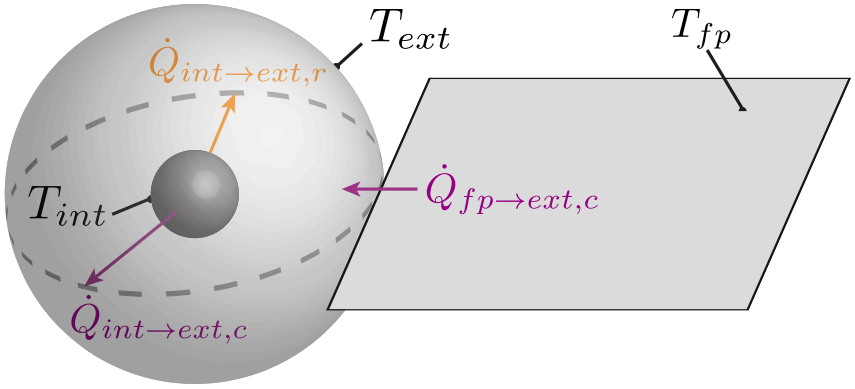

Supervisor: Jonis Kiesbye
Chair of Astronautics
Technische Universität München

Erklärung

Ich erkläre, dass ich alle Einrichtungen, Anlagen, Geräte und Programme, die mir im Rahmen meiner Semester- oder Masterarbeit von der TU München bzw. vom Lehrstuhl für Raumfahrttechnik zur Verfügung gestellt werden, entsprechend dem vorgesehenen Zweck, den gültigen Richtlinien, Benutzerordnungen oder Gebrauchsanleitungen und soweit nötig erst nach erfolgter Einweisung und mit aller Sorgfalt benutze. Insbesondere werde ich Programme ohne besondere Anweisung durch den Betreuer weder kopieren noch für andere als für meine Tätigkeit am Lehrstuhl vorgesehene Zwecke verwenden.

Mir als vertraulich genannte Informationen, Unterlagen und Erkenntnisse werde ich weder während noch nach meiner Tätigkeit am Lehrstuhl an Dritte weitergeben.

Ich erkläre mich außerdem damit einverstanden, dass meine Master- oder Semesterarbeit vom Lehrstuhl auf Anfrage fachlich interessierten Personen, auch über eine Bibliothek, zugänglich gemacht wird, und dass darin enthaltene Ergebnisse sowie dabei entstandene Entwicklungen und Programme vom Lehrstuhl für Raumfahrttechnik uneingeschränkt genutzt werden dürfen. (Rechte an evtl. entstehenden Programmen und Erfindungen müssen im Vorfeld geklärt werden.)

Ich erkläre außerdem, dass ich diese Arbeit ohne fremde Hilfe angefertigt und nur die in dem Literaturverzeichnis angeführten Quellen und Hilfsmittel benutzt habe.

Garching, den 16. September 2022

_____

Unterschrift

Name: Johannes Koch

Acknowledgements

The analysis of orbit data and the correlation of a thermal simulation model would not have been possible without the work of many hundreds of students working on the MOVE-II project for over 6 years. Starting with everyone who contributed to the design, building and launch of the satellite, up to each one who contributed in the development of its extensive digital twin.

Special thanks are due to the mission control team, which took the great effort to control the spacecraft over more than the last three years and were able to collect a huge amount of data, which represent the base for the study presented here. Despite many issues and the covid pandemic, they were able to keep their great work and therefore the satellite up.

I also would like to thank Jonis Kiesbye and David Messmann. They were always very helpful by giving advice on my work and by proposing new ideas.

Zusammenfassung

Der Satellit Munich Orbital Verification Experiment 2 (MOVE-II) ist ein von Studenten entworfener, gebauter und getesteter 1U-CubeSat aus dem Lehrstuhl für Raumfahrttechnik (LRT) der Technischen Universität München (TUM). Er wurde am 3. Dezember 2018 nach einer Entwicklungsphase von über drei Jahren gestartet. Seine Nutzlast besteht aus 4-Junction-Solarzellen, die in der erdnahen Weltraumumgebung getestet werden sollen.

Kurz nach dem Start musste zum einen festgestellt werden, dass die Kommunikation mit dem Satelliten nicht wie erhofft funktionierte und zum anderen, dass die Winkelgeschwindigkeit aufgrund einer ungünstigen Verlegung der stromführenden Kabel der Solarpaneele dazu neigt, sich stetig zu erhöhen. Dennoch konnte die Winkelgeschwindigkeit des Satelliten innerhalb von einigen Monaten auf ein normales Maß reduziert werden. Diese Regelung muss jedoch kontinuierlich durchgeführt werden, da der Satellit ansonsten dazu neigt, seine Winkelgeschwindigkeit stetig zu erhöhen. Nicht allein die Unfähigkeit des Satelliten über einen längeren Zeitraum hinweg im sunpointing Modus zu verweilen, führt zu einem instabilen Betrieb von MOVE-II. Auch sorgen deutlich niedrigere Temperaturen als vor dem Start prognostiziert dafür, dass die ohnehin knapp bemessene Batteriekapazität nicht ausreichend ist, um einen stabilen Betrieb im Erdschatten zu gewährleisten.

Besonders deutlich wird dies bei der hier durchgeführten Analyse der Orbitdaten. Seit dem Start des Satelliten sind zum jetzigen Zeitpunkt (Stand August 2022) bereits über drei Jahre vergangen. In dieser Zeit wurden dank des Mission Control Teams viele Daten über den Status des Satelliten und dessen Sensoren gesammelt, welche von MOVE-II empfangen wurden und in einer Datenbank abgespeichert. Ein Teil dieser wird im Rahmen dieser Arbeit analysiert. Diese Daten zeigen, dass die Betriebszeit des Satelliten nur selten über die Dauer eines Orbits hinausgeht und zudem über die Jahre stetig abgenommen hat. Dies deutet auf eine Degradation der Batterie hin, welche ebenfalls durch einen merklichen Anstieg des Innenwiderstands bestätigt werden konnte. Zudem wurde die Temperatur der Batterie über die gesamte Missionsdauer analysiert. Dabei erkenntlich geworden sind Schwankungen mit einer Periodizität von einem Jahr. Diese werden höchstwahrscheinlich durch eine Kombination aus dem Einfluss des elliptischen Erdorbits und einer Variation der Dauer des Satelliten im Erdschatten pro Orbit über das Jahr hinweg ausgelöst.

Über den Zeitraum der letzten Jahre wurde ein Simulationsmodell des Satelliten entwickelt, welches diesen in möglichst exakter Weise in Form von Lageregelung, Leistungselektronik und Temperatur nachbilden soll. Vor Allem die einfach gehaltene Thermalsimulation des „Digital Twins“ wurde anhand der Orbitdaten erfolgreich korreliert, mit dem Ergebnis, dass die Batterietemperatur mit einem durchschnittlichen Root Mean Square Error (RMSE) von 2.10 K vorhergesagt werden kann. Dieses Resultat siedelt sich im Vergleich mit der Korrelation von deutlich komplexeren Simulationsmodellen im oberen Genauigkeitsspektrum an. Erreicht wurde dies allein durch eine Anpassung der simulierten Emissivität und Absorptivität der Außenschale des Satelliten von ursprünglich $\epsilon_{ext,IR} = \alpha_{ext,sol} = 0.7$ auf $\epsilon_{ext,IR} = 0.79$ und $\alpha_{ext,sol} = 0.62$. Eine weit-

ere Modifikation des Wärmeübergangs zwischen des äußeren und inneren Knotens der Simulation, sowie eine Anpassung der spezifischen Wärmekapazitäten erbrachten keine weitere Verbesserung der Korrelation.

Abstract

The Munich Orbital Verification Experiment 2 (MOVE-II) satellite is a student-designed, built, and tested 1U-CubeSat from the Chair of Astronautics (LRT) of the Technical University of Munich (TUM). It was launched on December 3, 2018, after a development period of over three years. Its payload consists of 4-junction solar cells to be tested in the near-Earth space environment.

Shortly after the launch, it was found, first, that communication with the satellite did not function as anticipated and, second, that the angular velocity tended to increase steadily due to an unfavorable routing of the solar panels' current-carrying cables. Nevertheless, the satellite's angular velocity was reduced to a normal level within a few months. However, this regulation must be carried out continuously, otherwise the satellite tends to continuously increase its angular velocity. It is not just the satellite's inability to remain in sunpointing mode for an extended period of time that causes MOVE-II to operate unstably. Significantly lower temperatures than expected before launch also ensure that the already tight battery budged is not sufficient to guarantee stable operation in the Earth's shadow.

This becomes particularly clear in the analysis of the orbit data carried out here. At the present time (as of August 2022), more than three years have passed since the launch of the satellite. During this time, thanks to the mission control team, a lot of data about the status of the satellite and its sensors has been collected, which were received by MOVE-II and stored in a database. Some of these are analyzed as part of this work. The data shows that the operating time of the satellite rarely exceeds the duration of one orbit and has also steadily decreased over the years. This indicates a degradation of the battery, which could also be confirmed by a noticeable increase of the internal resistance. In addition, the temperature of the battery was analyzed over the entire mission duration. These are most likely caused by a combination of the influence of the elliptical Earth orbit and a variation of the duration of the satellite in the Earth's shadow per orbit over the year.

Over the period of the last few years, a simulation model of the satellite has been created to replicate it as accurately as possible in terms of attitude control, power electronics and temperature. Especially the simple thermal simulation of the "Digital Twin" was successfully correlated with the orbit data, with the result that the battery temperature can be predicted with an average Root Mean Square Error (RMSE) of 2.10 K. This result settles in the higher accuracy spectrum compared to the correlation of much more complex simulation models. This was achieved solely by adjusting the simulated emissivity and absorptivity of the satellite's outer shell from originally $\epsilon_{ext,IR} = \alpha_{ext,sol} = 0.7$ to $\epsilon_{ext,IR} = 0.79$ and $\alpha_{ext,sol} = 0.62$. Further modification of the heat transfer between the outer and inner nodes of the simulation, as well as an adjustment of the specific heat capacities did not yield any further improvement of the correlation.

Contents

List of Figures

List of Tables

Symbols

Symbol	Unit	Description
A	m^2	Area
a	-	Albedo
c	J/(kg K)	Specific Thermal Capacity
d	m	Diameter
F	-	View Factor
h	m	Thickness
I	A	Current
i	rad	Orbit Inclination
l	m	Length
m	kg	Mass
P	s	Orbit Period
$\dot{Q}$	W	Thermal Heat Flux
q	-	Quaternion
R	Ω or K/W	Resistance (electrical or thermal)
r	m	Radius
S_0	W/m^2	Solar Constant
T	K	Temperature
t	s	Time
U	V	Voltage
V	m^3	Volume
α	-	Absorptivity
β	rad	Beta Angle
ϵ	-	Emissivity
λ	W/(m K)	Thermal Conductivity
μ	m^3/s^2	Standard Gravitational Parameter
Ω	rad	RAAN
ω	1/s	Angular Velocity
ρ	kg/m^3	Density
σ	$W/(m^2 K^4)$	Stefan–Boltzmann Constant
Θ	rad	Right Ascension of the Sun

Acronyms

ADCS Attitude Determination and Control System

BCR Battery Charge Regulator

CDH Command and Data Handling system

COM Communications System

DCIR Direct Current Internal Resistance

ECI Earth-centered inertial

EPS Electrical Power System

JD Julian date

LRT Chair of Astronautics

LTAN Local Mean Time of Ascending Node

MOVE-II Munich Orbital Verification Experiment 2

MSE Mean Square Error

NORAD North American Aerospace Defense Command

OCV Open Circuit Voltage

PSLV Polar Satellite Launch Vehicle

RAAN Right Ascension of Ascending Node

RMSE Root Mean Square Error

SGP Simplified General Perturbations

SOC State of Charge

SOH State of Health

SSO Sun-Synchronous Orbit

STEP Space Technology Experiments Project

STSL Space Technology Synthesis Laboratory

TLE Two Line Element

TUM Technical University of Munich

TVAC Thermal Vacuum

UVP Under-Voltage Protection

WARR Scientific Workgroup for Rocketry and Spaceflight (German: Wissenschaftliche Arbeitsgemeinschaft für Raketentechnik und Raumfahrt)

1 Introduction

Since the late 1990s, CubeSats gained in popularity from their first appearance until today. The size of the satellite worked with in the following is a 1U-CubeSat. This means, that the satellite is one *unit* in size, which translates to dimensions of 10x10x10 cm and a maximum weight of 2 kg. Multiples of this form factor also exist as 2U, 3U, up to 12U-CubeSats. [1]

A mayor advantage of CubeSats compared to other, larger satellites, is the light weight and the possibility to launch the satellite as a secondary payload, together with other missions. This greatly reduces the launch cost and is one reason why CubeSats are so popular today. Together with the always continuing miniaturization of electronics, a shift from the exclusive use in research and student projects towards the commercialization of CubeSats could be observed.

The following should provide an overview over most of the background knowledge needed to understand the intentions behind and the necessity of this study.

1.1 The MOVE-II Satellite and Its Problems

The MOVE-II satellite is a student run project of the Scientific Workgroup for Rocketry and Spaceflight (German: Wissenschaftliche Arbeitsgemeinschaft für Raketentechnik und Raumfahrt) (WARR) and the Chair of Astronautics (LRT) at Technical University of Munich (TUM), which had and still has the main goal of educating students on developing a satellite and operating it consistently.
After a development, building and testing phase of over 3 years by over 200 students, the 1U-CubeSat launched on December 3 in 2018 onboard the SSO-A launch on a Falcon-9 rocket into a Sun-Synchronous Orbit (SSO). As a payload it features a 4-junction solar cell, provided by AZUR SPACE, in order to test it in the space environment. It is situated on the Toppanel, which can be found in the explosion drawing in Figure 1–1. [2]

As it can be clearly seen in Figure 1–1, the CubeSat is surrounded by a Toppanel on top, four Sidepanels on the sides and an S-Band antenna on the bottom. Furthermore there are UHF and VHF antennas extending from the bottom of the satellite.
Additionally four Flappanels help with maximizing the surface of the solar cells when pointing to the Sun. They are hinged to the top part of each Sidepanel and once the satellite is deployed they ”flap” out in order to fulfill the space limitation for a 1U CubeSat while in the launch vehicle. On each of the Flappanels two 4-junction solar cells are mounted, with a maximum power per cell of 1.2 W respectively. More triple-junction solar cells can be found on the Sidepanels, able to produce 1.2 W per panel [4].
A 20 Wh battery and an Electrical Power System (EPS) are situated in the middle of the satellite. Both these parts were supplied by Clyde Space.

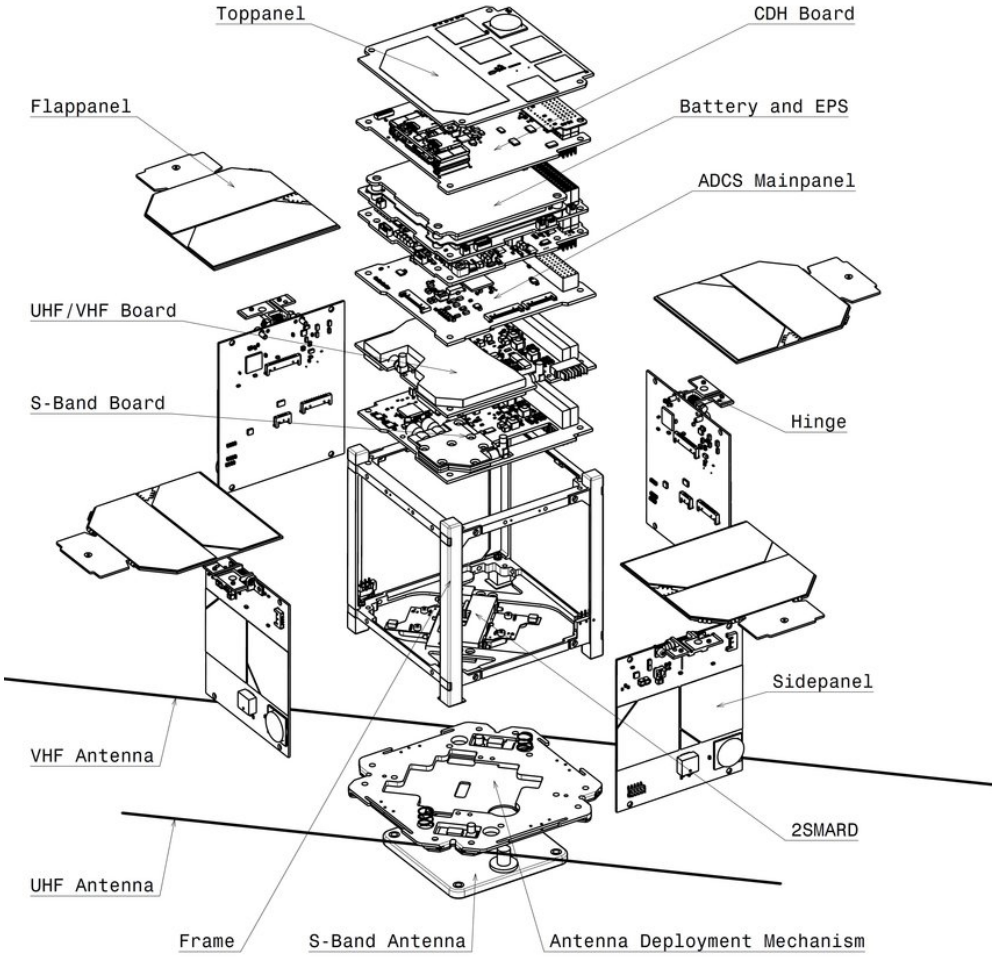

Fig. 1–1: Explosion drawing of MOVE-II [3]

1.1.1 High Turn Rates

A month after launch, it became clear that the satellite was spinning at a speed of about 200 °/s. This number increased up to over 500 °/s, before the Attitude Determination and Control System (ADCS) could be modified in a way to reduce the spin rate to a normal amount. A spin rate less than 10 °/s was first achieved on May 29 2019. The reason for this tendency to spin up to uncontrollable speeds is most probably a design issue. Due to a current loop, formed by current-carrying wires underneath the Flappanels, a magnetic dipole moment is induced when sunlight is shining on the solar cell above. Without any interference from the ADCS, the satellite will spin itself up to uncontrollable speeds. [2]
These high spin rates also significantly interfere with the communication from the ground station in Garching to the satellite. Therefore much of the data received is corrupted or not complete.

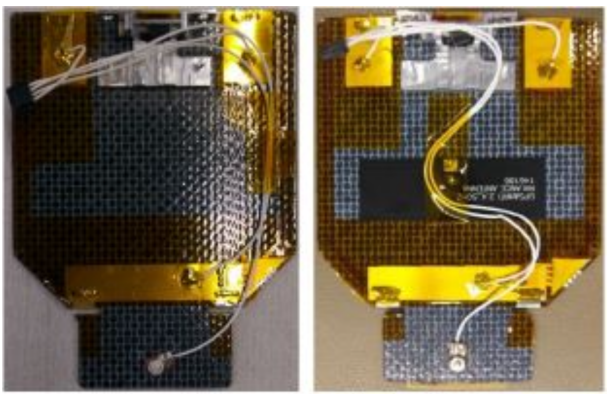

Fig. 1–2: Solar Cell Wiring Underneath the Flappanels of MOVE-II (left) and MOVE-IIb (right) [2]

Since this hardware issue could not be resolved remotely, a second, almost identical satellite, called MOVE-IIb was built and launched into space on July 5, 2019. Besides some improvements in the ADCS, the main difference to its predecessor was an optimized solar cell wiring in order to prevent a magnetic dipole induction. The difference in wire routing can be seen in Figure 1–2.

Unfortunately, MOVE-IIb was never truly operational, since no sufficient communication could be established to this date [5]. This could be due to a partial deployment of the Flappanels, resulting in undeployed antennae, or according to more recent studies, damaged transmitter hardware [6].

1.1.2 Negative Power Budget

Within the first months after launch of MOVE-II it became apparent that the 20 Wh battery installed in MOVE-II, could not keep up with the high power demands of the satellite, and the satellite therefore usually turns off during eclipse phases. This has several reasons, as also listed in [2]:
Firstly, the power consumption of essential subsystems is higher than expected due to an oversized Communications System (COM) transceiver and a misleading datasheet of the EPS. Secondly, the temperature of the satellite is much lower than expected, therefore the battery heater is activated for longer periods of time and its capacity is reduced due to a higher internal resistance. Furthermore MOVE-II is not able to stay in Sun-pointing mode reliably. Therefore the great surface of solar cells on the Toppanels is unlikely to produce its maximum power.

Frequent shutdowns during eclipse are the result of the negative power budget, caused by the intervention of the Under-Voltage Protection (UVP), in order to protect the battery when the capacity of the same drops below a certain level. Due to this behaviour a consistent control of the satellite for several orbits is not possible.

1.2 Orbit Data Analysis

One of the main chapters in this paper (chapter 4) attempts to correlate and analyze the orbit data received by the satellite from launch to this day. The goal behind it is to find interesting repeating or matching patterns between different sensor measurements and other data and to find suiting explanations for the occurrence and causation of these. For instance, especially the battery temperature, its internal resistance, and the satellites uptime are studied in detail.

1.3 Thermal Simulation of a Satellite

Thermal simulations are a critical step in the design of a satellite. They are an essential element in making good design decisions because the temperatures to which critical subsystems of the satellite are exposed are highly dependent on the materials used to build and insulate the satellite itself.

1.3.1 Thermal Environment

The satellite as a whole is influenced by its thermal environment, which consist of various forms of radiation exchange. For a satellite in orbit around another planet with a certain temperature, this planet can be seen as a black body radiator and is thus emitting infrared radiation, which will be absorbed by the satellite. Besides the obvious source of heat by the direct sunlight, also the reflected sunlight by the planet has to be considered. Furthermore the spacecraft itself is also emitting heat as a black body radiator, which helps to keep the satellite in an optimal temperature range. This simplified thermal environment is depicted in Figure 1–3.

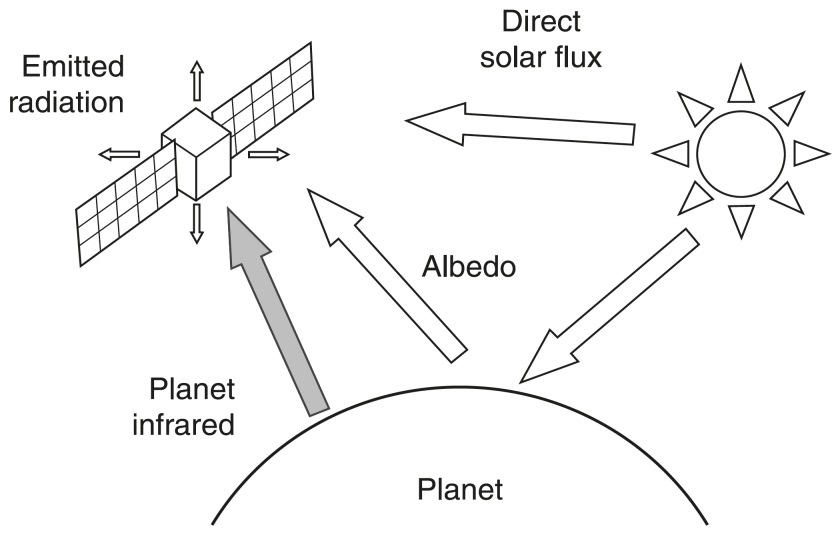

Fig. 1–3: Thermal Environment [7]

1.3.2 Internal Heat Flow

For the internals of the satellite only radiative and conductive heat flow are considered, since convection is not possible due to the absence of an atmosphere.
In order to model the temperatures of different parts of the spacecraft accurately, it has to be divided into several nodes i, each with its own thermal parameters, such as emissivity, absoprtivity, and thermal capacity C_i. Besides that thermal resistances between nodes have to be known. Knowing all heat fluxes and initial conditions, each nodes temperature T_i can then be calculated with the following differential equation:

$$C_i \cdot \frac{dT_i}{dt} = \dot{Q}_i \tag{1–1}$$

Here $\dot{Q}_i$ is representing the sum of all heat fluxes into the node. The heat capacity can be further broken down to $C_i = c_{p,i} \cdot \rho_i \cdot V_i$, as a product of specific thermal capacity $c_{p,i}$ and mass of the node $m_i = \rho_i \cdot V_i$.

1.3.3 Thermal Simulation of MOVE-II

Normally very simple models with only a few thermal nodes are used for first estimations of the expected temperature range. Later on in the design process they get replaced by more complex models, in order to get more detailed prediction of the temperatures of each subsystem.
Nonetheless, in the following, a simple model with only three nodes will be adapted to the orbit data of the MOVE-II satellite. Although this reduces the resolution of the model significantly, it makes adjustments and thus fitting it to given temperature curves much easier. Especially the temperature of the battery is of major interest for obtaining a better overall model of the satellite, since it affects the overall satellite performance.

2 State of the Art

This chapter briefly focuses on the most recent scientific research and established methods which are of importance for this paper. Besides presenting different methods of calculating the internal resistance of batteries, relevant information on thermal simulations and their correlation with real data is given.

2.1 Calculation of Internal Battery Resistance

Ideally the Direct Current Internal Resistance (DCIR) of any battery has to be measured in a controlled environment with constant conditions. In order to calculate the DCIR of a battery, the Open Circuit Voltage (OCV) U_{OC} has to be measured. Furthermore its voltage under a known load U_L is required. Knowing U_{OC}, U_L, and the resistance of the known load R_L, the DCIR of the battery can be calculated as follows:

$$R_{bat} = \left(\frac{U_{OC}}{U_L} - 1 \right) \cdot R_L \tag{2–1}$$

This method is normally chosen due to its robustness, because highly accurate measurements of voltage are easily accessible.

Another way of calculating the DCIR of a battery is through measuring its voltage drop ΔU, caused by a change in the current draw ΔI, according to Ohm's law. This method is also proposed by the norm IEC 61960 [8], in order to determine the DCIR of lithium batteries for portable devices.

$$R_{bat} = \frac{\Delta U}{\Delta I} = \frac{U_1 - U_2}{I_2 - I_1} \tag{2–2}$$

Using this method, a highly accurate measurement or estimation of the current draw is necessary. However, there is no need to measure the OCV, thus enabling the calculation of a voltage dependent DCIR.

2.2 Thermal Simulation of Small Satellites

In order to simulate the temperature of all relevant subsystems of a satellite over time, an integrator-based approach was used in this paper. There are other alternatives that require less computational effort, like the use of interpolation, but these deliver poor accuracy and uncertain predictions. [9]

A satellite that is very close to the MOVE-II satellite in terms of its size, is the SwissCube. This 1U-CubeSat was developed and built entirely in Switzerland as a collaboration of several educational institutions, led by the Ecole Polytechique Federale de Lausanne. It was launched September 23, 2009 onboard the Indian launcher Polar Satellite Launch Vehicle (PSLV)-C14 together with the Oceansat-2 Indian spacecraft. As the main objective of MOVE-II was to educate students by developing a whole satellite on their own, this also accounts for SwissCube. Besides that, the satellite should

have been able to show that the airglow emissions could be detected by an off-the-shelf detector, thus functioning as a cheap Earth sensor. However, this goal was not achieved. [10]
As Rossi and Ivanov have proven in [10], SwissCube's battery temperature can be modeled to a good accuracy with the use of only two thermal nodes. Their model consist of two concentric spheres: the outer one is representing the exterior of the satellite and the inner is intended to mirror the battery's temperature.
As a thermal environment, the model for SwissCube uses the same as explained before in subsection 1.3.1. Interestingly the eclipse phase was not modeled by simply removing the solar radiation from their equations, but rather varying it in a 60 %-100 %-60 % pattern. This behaviour was taken from the orbit data and implemented into the model for better results.
With their simple thermal model of the CubeSat they were able to yield a maximum temperature deviation of 3.0 °C compared to the orbit data. This proves that a simple thermal model is not equal to bad quality of the same, far from it! A model like this can be very helpful during the beginning of designing a new satellite and also during its lifetime by providing simple to correlate reference data.

Although the team of Rossi and Ivanov [10] had orbit data of almost 4 years available in order to correlate their model, only data from one single day was used to tune and validate their thermal model of the satellite. This however can lead to overfitting, which is why this paper aims on adapting the thermal model of MOVE-II to the orbit data of several years with more than 30 data sets in total.
Another important difference between MOVE-II and SwissCube is, that MOVE-II additionally is equipped with 4 Flappanels, as described before in section 1.1. Therefore a third node is added, to its model, which will be discussed in further detail in one of the next chapters 3.2.1.

2.3 Correlation of Thermal Models

Thermal models of satellites normally consist of hundreds to thousands of nodes. To these, the model of the 1U-CubeSat of the Space Technology Experiments Project (STEP) Cube Lab from the Space Technology Synthesis Laboratory (STSL) of Chosun University in South Korea also belongs. It consist of 420 nodes and thus represents every subsystem of the satellite in great detail. The correlation was conducted with Thermal Vacuum (TVAC) test data. The correlation criteria were a temperature difference of less than ± 3 °C for at least 90 % of the correlated subsystems. They were able to achieve their goal by adjusting the calculated conductivity and by lowering the heat dissipation of the battery by over an order of magnitude. [11]

Another interesting correlation attempt was performed by Hannemann on the MOVE-II satellite, which is also in the focus of this paper. Prior to launch, the thermal dynamics were simulated in an ESATAN-TMS® model with 2597 nodes and verified using steady state TVAC tests. After launch, deviations of around 30 °C from the estimated temperatures could occur. Therefore, a correlation was performed, aiming at reducing this discrepancy as far as possible. By a combination of altering the internal power dissipation, the specific thermal capacity, the thermal conductivity and the optical properties

of the satellite, a reduction of the temperature difference could be achieved. However the results were still far from optimal, since for example the battery temperature was still off by around 15 °C from the orbit data. [12]

3 Methodology

This chapter will focus on the approach used in this paper of conducting the orbit data analysis and how the digital twin was correlated to represent the real satellite as close as possible.

3.1 Orbit Data Analysis Methods

The data received by the satellite is stored in a PostgreSQL-database, divided into the different subsystems. In order to study the collected information, several MATLAB®-scrips were used in combination with the *Database Explorer* App and associated functions [13]. With the help of these tools, the battery temperature, its internal resistance, and the satellites uptime are analyzed and examined in chapter 4. In the following, the necessary methods are presented.

3.1.1 Preparation of Battery Temperature Data

As a result of slow link speeds between the ground station in Garching and the satellite as well as a short overflight window, the raw data received from the satellite was of inconsistent quality, characterized by a lot of outliers and missing values. In order to achieve good results, it was necessary to perform a variety of operations. First, impossible temperature readings that were well outside of the satellite's normal operating range were filtered out, using the `rmoutliers` function provided by Matlab. Due to the irregularity in time of the data, a daily mean temperature was calculated, with the use of `retime`. Finally these mean values were smoothed with a Gaussian-weighted moving average filter implemented in `smoothdata`.

3.1.2 Computation Method of Internal Battery Resistance

The internal battery resistance, also referred to as DCIR (R_{bat}), can be calculated in different ways, as mentioned in section 2.1. As the environment of the battery can not be controlled on the satellite, it varies greatly in temperature. Furthermore the current draw can not be regulated, so no OCV (U_{OC}) can be measured, as this would involve disconnecting the battery from the rest of the system. As this is not an option for a satellite in orbit, the internal resistance is estimated from measurements of voltage and current acquired during the operation of MOVE-II.

Voltage U_{bat} and current I_{bat} of the battery are measured at its terminals by the EPS board. In order to compute an approximation of R_{bat}, temporally adjacent data pairs of U_{bat} and I_{bat} measured at the battery's terminals by the EPS are compared to each other. This is done by applying the method proposed by norm IEC 61960 [8] in Equation 2–2. The resulting iterative equation is illustrated in Equation 3–1. Aiming to receive more accurate results, only current readings between 50 mA and 500 mA, and voltages greater than 5 V were considered. These limits represent the nominal oper-

ating range of the satellite, and aim to eliminate non-linearities in the voltage drops caused by varying current draw.

$$R_{bat,i} = \frac{U_{bat,i-1} - U_{bat,i}}{I_{bat,i} - I_{bat,i-1}} \tag{3–1}$$

To minimize influences on the internal resistance by changing SOC values, only data pairs of voltage and current with a maximum temporal separation of one minute were compared. Furthermore values ≤ 0 or unreasonable high values of > 10 were filtered out in favour of more realistic results. In order to decrease spikes in the final results, the MATLAB® function `rmoutliers` was used to remove outliers in the upper 10th percentile range.

By filtering the input data pairs of voltage and current for specific temperature or voltage levels, it is possible to obtain estimates of the DCIR as a function of these values.

3.1.3 Verification of the Internal Battery Resistance Calculations

In order to verify the calculated resistance values, a Simulink® model of the battery was used. This model was isolated from the digital twin in order to simplify the way of feeding it with optimized data in a controlled way. The model itself is shown in Figure A–1. The inputs are: Power draw from the satellite systems or charging from the solar cells, as well as the current battery temperature. These inputs were modeled using sine wave generators and step generators with different amplitude and frequency, matching the orbital rhythm. Furthermore a little noise was added to the input power.

The battery itself consist of a discrete integrator with a saturation limit of 20 Wh and an initial charge of 5 Wh. Open-circuit voltages were simulated by a lookup table, fed with the SOC of the battery. Finally, the internal battery resistance, depending on its temperature T, was modeled according to Equation 3–2, which was obtained through measurements on ground. The resulting voltage drop was subtracted from the open-circuit voltage. Temperature, voltage and current of the battery were recorded with a rate of 1/min, just like the orbit data. In case of the current measurements the resolution of the signal was also limited to a step size of 15 mA, as the same behavior was observed in the data received from MOVE-II. The model also features an UVP, just like the real satellite does. When a voltage of $\leq$ 6.2 V is reached, the UVP turns on and the power draw from the satellite is limited to 0.1 W, which is intended to simulate the power consumption of the maximum power point trackers still active in the ”off state”. Once the battery reaches a voltage of 8 V, the UVP is turned off again and the power consumption is no longer restricted. In the next step, the output of the model was fed into the same scripts, used for the analysis of the actual orbit data. The aim here being the recreation of the DCIR as a function of temperature with only the voltage and current readings, simulated by the Simulink® model.

$$R_{bat}(T) = 11.93\,\Omega - 0.039\,\frac{\Omega}{\mathrm{K}} \cdot T \tag{3–2}$$

3.1.4 Data Preparation for Uptime Analysis

In order to analyze the uptime of the satellite, the provided data first has to be prepared, to make it more easily understandable and displayable.
As the recorded data is a series of upwards counting integers, the first step in data preparation is to filter out all intermediate values, which are essentially redundant, such that only the maxima remain. Furthermore, it is checked whether the values are actually within the range of the possible. Since the recording date is known, the difference in time between two uptime values must not exceed the value of the uptime itself, thus eliminating faulty data. Furthermore a monthly mean of the maximum uptimes was calculated by the use of the `retime` function, provided by MATLAB®.

3.2 Thermal Simulation Model and Correlation Methods

The following gives a detailed description to the thermal model used to mirror the temperature of the battery, integrated into MOVE-II. Furthermore the methods applied in order to correlate this model are presented. This includes the initial conditions, the preparation of the orbit data, the fit algorithm needed to compare results, and finally the correlation strategy.

For the here presented thermal model, the Simulink® model described in [14] by Jonis et al. was used as a base.

3.2.1 Thermal Model

The thermal model of MOVE-II consists of only three nodes. As stated by Pérez-Grande et al. [15], and Rossi and Ivanov [10], a model with only two nodes is sufficient for supporting the design process of a small satellite of cubic form. Since MOVE-II has additionally 4 Flappanels, which extend from the sides of the Toppanel, compared to the SwissCube introduced in section 2.2, a third node was added to the thermal model for increased accuracy, which is supposed to represent these panels, which are carrying some of the solar cells.

Since the model is not specifically complex and is getting a lot of environmental data from the rest of the simulated satellite, the thermal model was also implemented in the Simulink® simulation, as already described in [14]. In this way, full control over the simulation can be ensured and the analysis of the output data is very convenient by the use of Matlab®.

As stated before, the model consists of three nodes: an inner solid sphere (int) with a diameter of 0.09 m, an outer hollow sphere (ext) with an outer diameter of 0.11 m and an inner diameter of 0.107 m, and four 10x10x0.1 cm Flappanels, modeled as one node (fp). This is also illustrated in Figure 3–1.
By modeling the CubeSat's outer shell as a sphere, rather than a cube, it can be assumed, that the surface temperature of the satellite is homogeneous. Thus modeling it as a single node is possible. In this case the internal sphere is representing the innermost component of MOVE-II – the battery. It is thermally coupled to the outer sphere by conduction $\dot{Q}_{ext\rightarrow int,c}$ and radiation $\dot{Q}_{ext\rightarrow int,r}$. The Flappanels on the other

hand are only conductively coupled to the outer sphere $\dot{Q}_{ext\rightarrow fp,c}$ through a hinge with defined cross-sectional area A_h and length l_h. Here, radiative heat transfer from the Flappanels to the exterior can be neglected, due to a very small viewing factor between the two and therefore low heat transfer by radiation in comparison to conduction.
All parameters used in the thermal model and the following equations can be found in section A.1. Physical correlations were taken from [16].

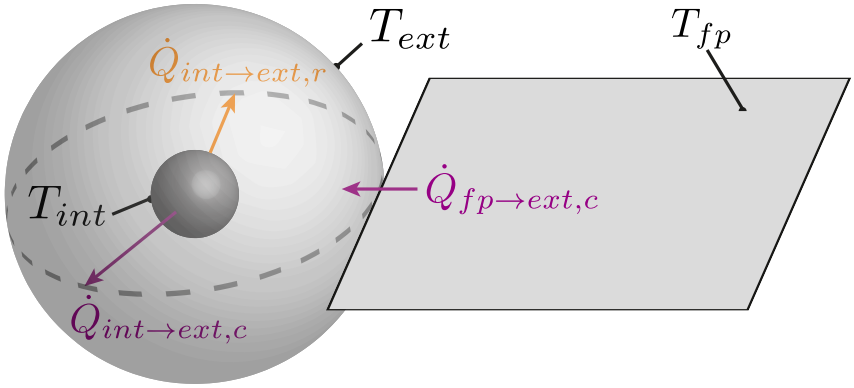

Fig. 3–1: Structure of the Thermal Model and Internal Heat Flow

Besides the radiation and conduction of the outer shell, the inner node is only directly affected by an internal heat source $\dot{Q}_{P,loss}$. It is composed of the power dissipation inside the battery, inside the Battery Charge Regulators (BCRs), inside the ADCS and general power consumption. The external node $\dot{Q}_{ext}$ and the Flappanels $\dot{Q}_{fp}$ are also under influence of internal heat sources $\dot{Q}_{P,body}$ and $\dot{Q}_{P,sol}$, respectively, resulting from losses on the outside of the satellite and inside the solar panels.

$$\dot{Q}_{int} = \dot{Q}_{ext\rightarrow int,r} + \dot{Q}_{ext\rightarrow int,c} + \dot{Q}_{P,loss} \tag{3–3}$$

$$\dot{Q}_{ext} = -\dot{Q}_{ext\rightarrow int,r} - \dot{Q}_{ext\rightarrow int,c} - \dot{Q}_{ext\rightarrow fp,c} + \dot{Q}_{env\rightarrow ext} + \dot{Q}_{P,body} \tag{3–4}$$

$$\dot{Q}_{fp} = \dot{Q}_{ext\rightarrow fp,c} + \dot{Q}_{env\rightarrow fp} + \dot{Q}_{P,sol} \tag{3–5}$$

with

$$\dot{Q}_{ext\rightarrow int,r} = \frac{\sigma \cdot A_{int} \cdot (T_{ext}^4 - T_{int}^4)}{(\frac{1}{\epsilon_{int,IR}} + \frac{A_{int}}{A_{ext,inner}})(\frac{1}{\epsilon_{ext,IR}} - 1)} \tag{3–6}$$

$$\dot{Q}_{ext\rightarrow int,c} = \frac{T_{ext} - T_{int}}{R_{ext\rightarrow int}} \tag{3–7}$$

$$\dot{Q}_{ext\rightarrow fp,c} = \frac{T_{ext} - T_{fp}}{\frac{l_h}{\lambda_h \cdot A_h}} \tag{3–8}$$

The conductive heat transfer from the external to internal node $\dot{Q}_{ext\rightarrow int,c}$ is controlled by the thermal resistance between them $R_{ext\rightarrow int}$. It is the sum of the thermal resistance of eight aluminium carriers R_{al} and the thermal resistance of the solder mask R_{mask}:

$$R_{ext\rightarrow int} = R_{al} + R_{mask} \tag{3–9}$$

with

$$R_{al} = \frac{\frac{d_{ext,inner} - d_{int}}{2}}{\lambda_{al} \cdot A_{ext \to int,c}} \tag{3–10}$$

and

$$R_{mask} = \frac{h_{mask}}{\lambda_{mask} \cdot A_{ext \to int,c}} \tag{3–11}$$

Furthermore, the external and Flappanel nodes are also influenced by the near-Earth space environment $\dot{Q}_{env \to i}$, depicted in Figure 1–3. It is composed of solar irradiance $\dot{Q}_{sun \to i}$, the Earth's albedo $\dot{Q}_{albedo \to i}$ and its infrared radiation $\dot{Q}_{IR \to i}$, as well as thermal dissipation to space $\dot{Q}_{i \to space}$:

$$\dot{Q}_{env \to ext} = -\dot{Q}_{ext \to space} + \dot{Q}_{sun \to ext} + \dot{Q}_{albedo \to ext} + \dot{Q}_{IR \to ext} \tag{3–12}$$

$$\dot{Q}_{env \to fp} = -\dot{Q}_{fp \to space} + \dot{Q}_{sun \to fp} + \dot{Q}_{albedo \to fp} + \dot{Q}_{IR \to fp} \tag{3–13}$$

with

$$\dot{Q}_{i \to space} = \epsilon_{i,IR} \cdot \sigma \cdot A_i \cdot T_i^4 \tag{3–14}$$

$$\dot{Q}_{sun \to i} = \delta_{sun} \cdot \alpha_{i,sol} \cdot A_{i\perp} \cdot S_0 \tag{3–15}$$

$$\dot{Q}_{albedo \to i} = \delta_{sun} \cdot \alpha_{i,sol} \cdot A_{i\perp} \cdot a \cdot F_{i \to albedo} \cdot S_0 \tag{3–16}$$

$$\dot{Q}_{IR \to i} = \alpha_{i,IR} \cdot \sigma \cdot A_{i\perp} \cdot F_{i \to earth} \cdot \epsilon_{earth,IR} \cdot (T_{earth}^4 - T_i^4) \tag{3–17}$$

As the background radiation is approximated to be 0 K here, $\dot{Q}_{i \to space}$ only relies on the temperature of the node T_i. The direct and indirect radiation form the Sun $\dot{Q}_{sun \to i}$ and $\dot{Q}_{albedo \to i}$ are turned *on* or *off* by the multiplication of δ_{sun}, which is either 1 or 0, respectively. Per Kirchhoff's law [17], $\alpha_{i,IR}$ can be replaced by $\epsilon_{i,IR}$ in the last Equation 3–17.

According to the heat Equation 1–1, the temperature of each node i can finally be calculated by:

$$T_i = \int \frac{\dot{Q}_i}{C_i} dt \tag{3–18}$$

3.2.2 Initial Conditions

The initial temperature of each node T_i is set according to the received orbit data in a way that all three temperatures T_{int}, T_{ext} and T_{fp} are equal to the first temperature reading of the battery temperature T_{bat} obtained from the orbit data in the simulated time slot.

The initial attitude of the satellite is chosen to be $q_{bi,0} = [1\ 0\ 0\ 0]$, which does not have a great affect on the simulated temperature, since MOVE-II is simulated in a tumbling state over all three axes with an initial angular velocity of $\omega_{b,bi,0} = [0.1\ 0.1\ 0.1]$ /s. Simulations of higher turn rates, as MOVE-II normally experiences them, were not feasible since simulation times would increase to an unjustifiable level. However this is not a serious issue, since the two main nodes are radially symmetric and thus only influenced in an asymmetric way by the third node, representing the Flappanels.

The orbit position is calculated by an Simplified General Perturbations (SGP) orbit propagator (here: SGP4) with a Two Line Element (TLE) and Julian date (JD) as initial conditions. The TLEs were taken from the North American Aerospace Defense Command (NORAD) through `www.space-track.org`, whereas the JD is calculated from the timestamp of the first data record in the given data set with the help of the function `juliandate` in Matlab®. Furthermore, the ADCS system was deactivated in the simulation.

3.2.3 Data Preparation

As mentioned in subsection 1.1.2, the satellite is suffering from UVP shutdowns in most eclipse phases. During this time the Command and Data Handling system (CDH) freezes and as a consequence the clock stops. Due to this circumstance the recorded time stamp in the telemetry data can have a substantial offset from the actual time. In order to get a good fit it is therefore mandatory to measure this offset in relation to the simulation model.
This is done by running the simulation with approximated parameters and comparing the results to the orbit data. By measuring the time difference between the turning points of the temperature curves, i.e. the transition into or out of the Earth's shadow, the offset can be determined very precisely and is added to the initial JD of the simulation for further simulations.

3.2.4 Fit Algorithm

After simulation, the obtained data is processed through a Matlab® script and compared to the orbit data. This is done by an evaluation of the RMSE. Because the RMSE is measured in the same variable as its response variable, it was preferred over the Mean Square Error (MSE). The RMSE of n data points is calculated by:

$$\text{RMSE} = \sqrt{\frac{\sum_{i=1}^{n}(y_i - \hat{y}_i)^2}{n}} \tag{3–19}$$

with y_i being the simulated values and $\hat{y}_i$ representing the expected orbit data.

Furthermore a difference in gradient between the orbit data and simulated data is calculated by the `polyfit` function by setting the polynomial degree to 1. This value can be used to determine if the trend of the temperature curve is similar to the orbit data's but should be regarded with caution since the orbit data is not guaranteed to be placed equally in time and is often characterized by missing data points. Hence the calculated gradient could be misleading.

3.2.5 Correlation Strategy

A set of parameters has to be approximated and then correlated in order to get a good temperature fit of the simulation. The first step therefore is to make educated guesses on the values of these parameters with the help of known component properties and valid assumptions in thermal modeling. This however was already done prior to the

work presented in this thesis. The initial parameters are collected in Table A–1. In the next stage these initial parameters have to be altered in a way, so that the RMSE of the simulated battery temperature, as well as the difference in gradient are minimized.
As there are many data sets available (see Table A–3) but only limited computing resources, one data set with high density of data records and as long a period as possible is chosen to perform an initial sensitivity analysis to certain parameter changes. Once an optimal fit is found, the updated simulation is computed for more data sets. Now the fine tuning begins, as the same parameters are varied once again, but on a smaller scale, for all simulations. For these simulation runs the fit value is averaged between all simulations with the same parameter sets. In this way it is possible to find the parameter set with the best overall fit, thus avoiding overfitting to one specific set of telemetry data.
A good telemetry data set to use for the initial sensitivity analysis of the battery temperature is data set 21-08 (see Table A–3), shown in Figure 3–2. It stretches over a period of about 5 orbits and has a high and uniform data density, which allows for an accurate linear trend calculation.

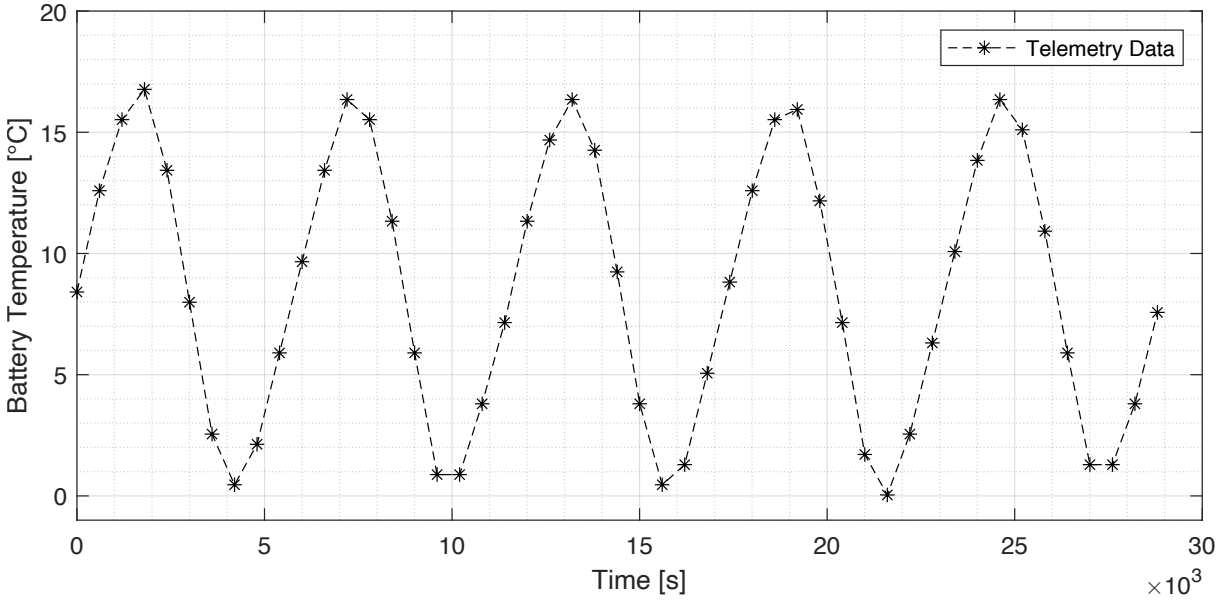

Fig. 3–2: Battery Temperature of Data Set 21-08

The parameters altered in the following section 5.1 in order to obtain the best fit on the orbit data are:

- Optical properties of the outer sphere, by altering its emissivity $\epsilon_{ext,IR}$ and absorptivity $\alpha_{ext,sol}$
- Thermal resistance between the inner and outer sphere, influenced by the thermal conductivity of the solder mask λ_{mask} and the emissivity of the inner sphere ϵ_{int}
- Thermal capacitance, by modifying the specific thermal capacity of the internal node $c_{p,int}$ and the external node $c_{p,ext}$

In order to simulate a different set of parameter combinations and analyze the results in an efficient way, these Simulink® simulations were executed in parallel with the help of the Parallel Computing Toolbox™ from Matlab®.

4 Orbit Data Analysis

With the help of the methods described in section 3.1, the orbit data received from MOVE-II over the duration of over three years are being analyzed in the following. Among them is the battery's temperature, the internal battery resistance, as well as the uptime of the satellite.

4.1 Battery Temperature

As the battery is one of the innermost components of MOVE-II, its temperature is of major interest. Due to its high thermal inertia and good thermal shielding by the rest of the satellite, it is assumed to be least prone to erratic temperature changes and more likely to represent the mean temperature of the satellite's internals.

4.1.1 Results

The orbit data received from the satellite was prepared by a series of operations presented in subsection 3.1.1, including the removal of outliers, calculating a daily mean and smoothing the resulting data. The results are shown in Figure 4–1, together with the raw data (excluding outliers).

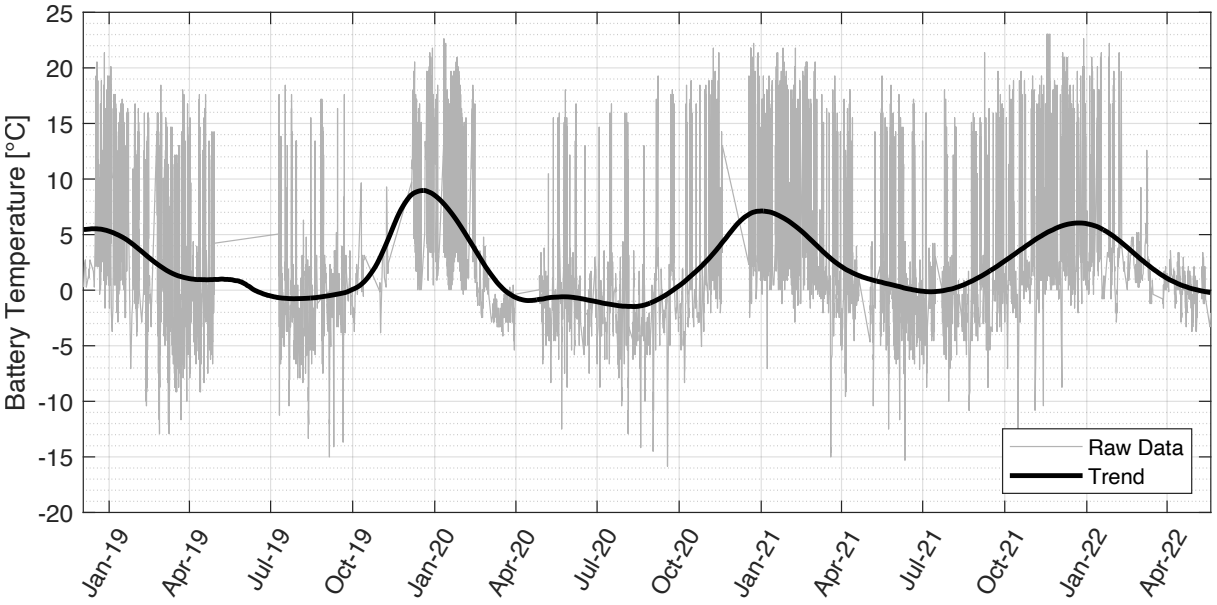

Fig. 4–1: Battery Temperature

4.1.2 Seasonal Dependence

From the processed data, shown in Figure 4–1, it is apparent that there is a seasonal variation in the temperature of the satellite. The maximum is reached between the

years in the months of December and January whereas the minimal temperature occurs in the months of June and July. In 2021 the average temperature was measured to be 3.0 °C with 6.4 °C from November to February and –0.6 °C from June to August. These seasonal differences of approximately 7.0 °C are mainly due to two causes: The Eccentricity of the Earth's orbit and the seasonal dependence of eclipse times in the SSO of MOVE-II. These two will be discussed in the following.

Another influence on the seasonal temperature variations of the satellite could result from the differences in the Earth's albedo between its northern and southern hemisphere, due to the difference in land cover. This however can be ruled out, since the difference in reflectivity between these two is compensated for by an on average denser cloud cover in the south, according to Datseris and Stevens [18].

4.1.2.1 Elliptic Earth Orbit

As Earth's orbit is not perfectly circular with an eccentricity of $e = 0.0167$ [19], the solar radiation arriving at our planet is subject to changes throughout the year. The Earth's aphelion on the orbit around Sun is time-wise located between July 4 and 5 with a distance to the Sun of around 1.017 au (1.52×10^{11} m) while its perihelion is located between January 2 and 5 with 0.983 au (1.47×10^{11} m) of distance [20]. This difference results in a variation of the solar constant S_0 from 1323 W/m^2 at aphelion to 1415 W/m^2 at perihelion, which corresponds to a change of almost 7 %. The fluctuations in solar activity however only have very little impact on S_0 of approximately 0.1 % [21] and are therefore not considered here.
With these values it is possible to calculate the steady state temperature of a spherical satellite, following the same trajectory as Earth. Assuming it is only irradiated by the Sun in the absence of a planet, with the cosmic microwave background temperature being approximately 0 K, the following formula for the satellite's temperature can be derived:

$$T_{sat} = \sqrt[4]{\frac{\alpha_{sol} \cdot S_0}{4 \cdot \epsilon_{IR} \cdot \sigma}} \tag{4–1}$$

With an absorptivity in the solar spectrum α_{sol} of 0.62 and an emissivity in the infrared spectrum ϵ_{IR} of 0.79 (derived in chapter 5) and the Stefan-Boltzmann constant $\sigma = 5.67 \times 10^{-8}$ W/(m^2 K^4) we get the following results:

- $T_{sat}(S_0 = 1415\,\text{W/m}^2) =$ –8.6 °C at perihelion
- $T_{sat}(S_0 = 1323\,\text{W/m}^2) =$ –13.0 °C at aphelion

Form this results a difference of 4.4 K between perihelion and aphelion. Although the circumstances are not the same as for transient temperature profiles normally encountered in satellites influenced by Earth's infrared radiation, albedo, and periodically shadowed by the same, this shows that the eccentricity of the Earth's orbit can, on average, have a noticeable effect on the satellite temperature.

4.1.2.2 Seasonal Dependence of Eclipse Times

Another influence on the temperature arises from the orbit of the satellite itself. As MOVE-II is orbiting Earth on an SSO, it is subject to slight variations in eclipse times. This can be proven by the following calculation:
As the eccentricity of MOVE-II's orbit is only $e = 0.0013$, we can assume a circular orbit for simplicity. From [22] we get the following formula for the *beta angle* β, which represents the angle between the solar vector and the orbit plane:

$$\sin\beta = \cos\Theta \cdot \sin\Omega \cdot \sin i - \sin\Theta \cdot \cos i_E \cdot \cos\Omega \cdot \sin i + \sin\Theta \cdot \sin i_E \cdot \cos i \tag{4–2}$$

with

- i Orbit inclination
- Ω Right Ascension of Ascending Node (RAAN) of the orbit
- Θ Angle in the ecliptic between the point of Aries and the direction to the Sun also known as right ascension of the Sun
- i_E Inclination of planet's equatorial plane relative to the ecliptic. $i_E = 23.44°$ for Earth

The eclipse time is then being calculated by

$$t_E = \frac{P}{\pi} \arccos \frac{\sqrt{r^2 - R^2}}{r \cdot \cos\beta} \tag{4–3}$$

with the Earth's Radius $R = 6378\,\text{km}$ and an orbit period of

$$P = 2\pi \cdot \sqrt{\frac{r^3}{\mu}} \tag{4–4}$$

for a circular orbit with the orbital radius r and the standard gravitational parameter $\mu = 3.986 \times 10^{14}\,\text{m}^3/\text{s}^2$ [16]. For the MOVE-II satellite with an orbital radius of $r = 6952.2\,\text{km}$ (obtained from the latest TLE on 11-06-2022), this results in durations of direct illumination by the Sun shown in Figure 4–2. Since MOVE-II is orbiting Earth on a SSO with a Local Mean Time of Ascending Node (LTAN) of 10 pm, its RAAN is changing with a rate of 2π per year, with its origin being the 292$^{\text{nd}}$ day of the year (October 19).

It can be seen that in fact the cold periods coincide with longer eclipse times, synonymous with shorter illumination times and vise versa. Admittedly, it is questionable whether this has a major effect on the temperature, since the difference between minimum and maximum is only 1.42 %, compared to the orbital period of MOVE-II (5769 s).

4.2 Internal Battery Resistance

The DCIR (here R_{bat}) is of great value for determining the battery's State of Health (SOH), as it increases linearly with the capacity available [23]. For this reason it is of major interest to obtain this value from the data, also with regard to future satellite missions. Unfortunately the environment of the battery is not controlled and varies

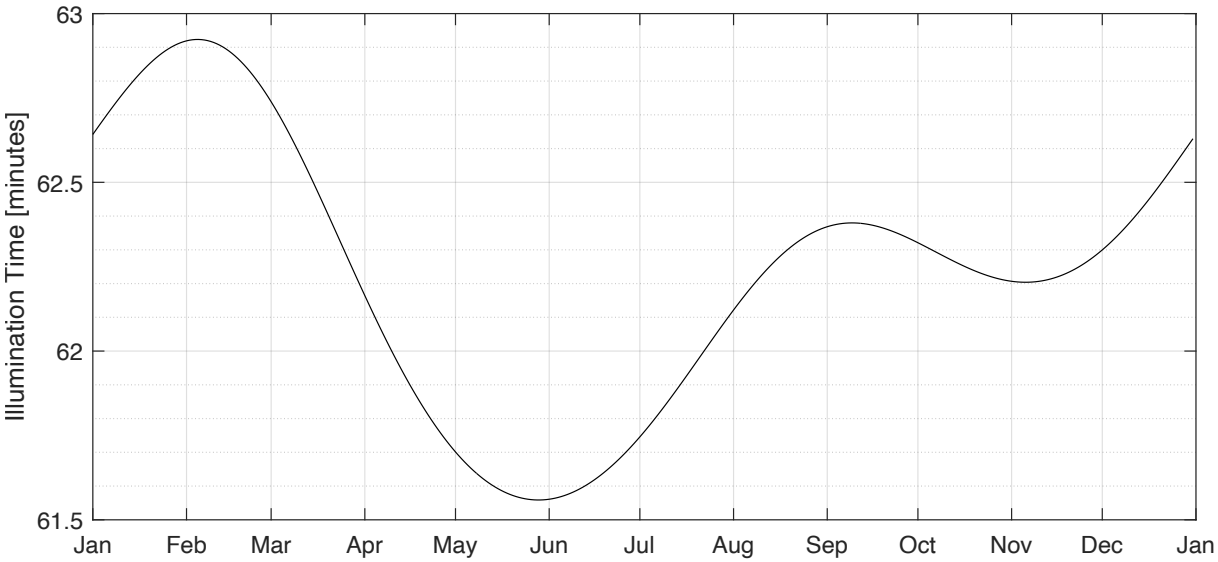

Fig. 4–2: Illumination Times of MOVE-II per Orbit

greatly in temperature. Furthermore the current draw can not be regulated, so no OCV (here U_{OC}) can be measured, as this would involve disconnecting the battery from the rest of the system. As this is not an option for a satellite in orbit, the internal resistance will be estimated from measurements of voltage, current and temperature acquired during the operation of MOVE-II below.

4.2.1 Results

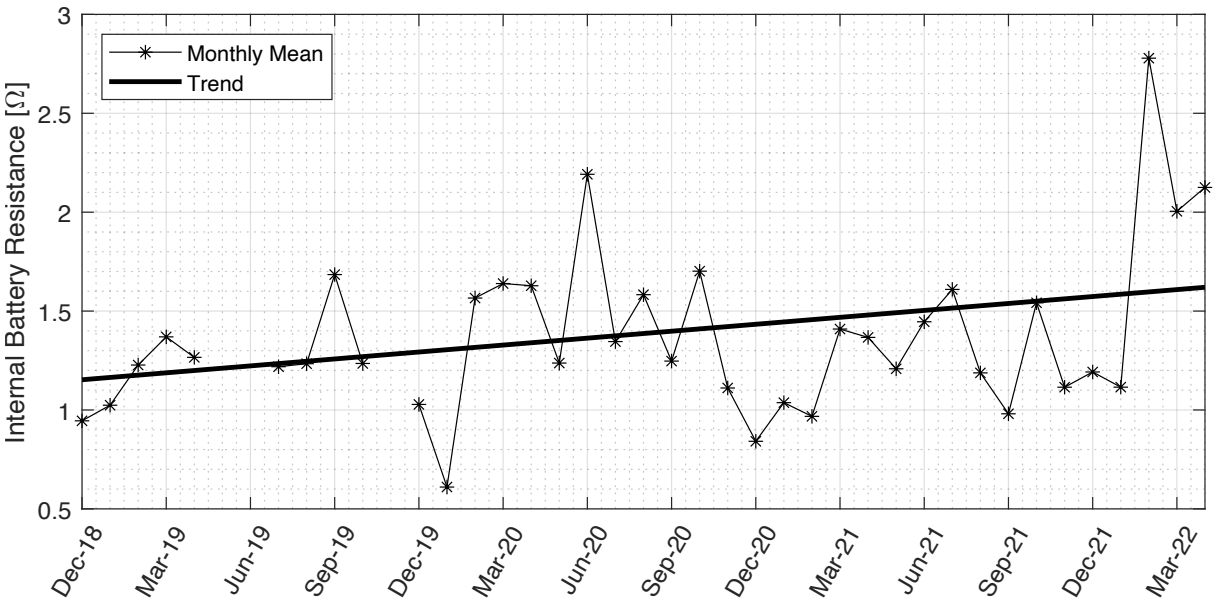

Fig. 4–3: Averaged Internal Battery Resistance

The results of the calculations, performed according to the method described in subsection 3.1.2, with the provided telemetry data can be seen in Figure 4–3. A slight

upwards trend of the resistance can be observed, with an increase of 140.4 mΩ per year. This is an expected effect, caused by the aging of the battery. Since it is exposed to very harsh environmental conditions, such as low average temperatures of 3.0 °C and rapid charging and discharging cycles [2], the battery's capacity shrinks as its internal resistance increases [24].

The restriction of the input data pairs for Equation 3–1 with respect to battery temperature or voltage levels, enables a determination of resistance values as a function of them. These analyses are presented below.

4.2.1.1 Temperature Dependent

By filtering out data-points with battery temperatures outside of an assumed range, it is very easy to obtain resistance values for that specific range. The only limitation being that there must be enough data points left after filtering, in order to produce reliable values for R_{bat}. Therefore, the range must not be chosen too small.
In this case the interval was chosen to be 5 K, with a lower limit of –15 °C and an upper limit of 25 °C, which corresponds to the total temperature range seen during operations (see Figure 4–1). Unfortunately there was not enough data to determine reliable results for temperatures from –15 °C to –10 °C.

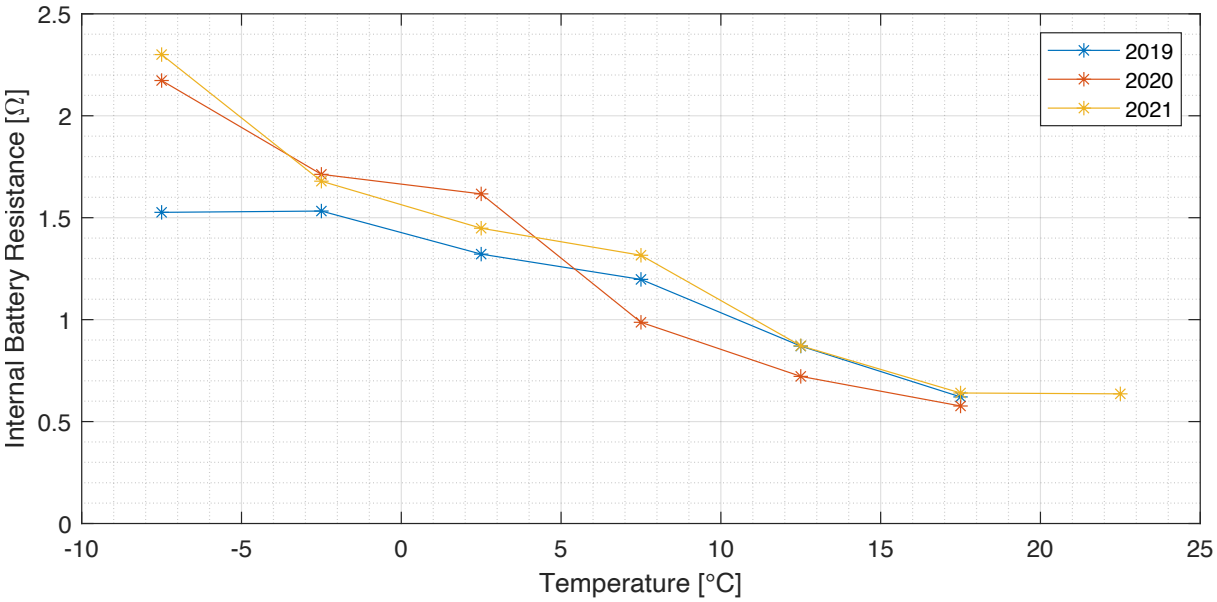

Fig. 4–4: Temperature Dependent Internal Battery Resistance

As it can be clearly seen in Figure 4–4, there is a significant relationship between the battery temperature and its resistance. Cold temperatures do correspond to high resistance, while higher temperatures signify lower resistances. Likewise, an increase in resistance can be observed over time. This can be seen particularly well in the lower temperature ranges, whereas no significant difference can be detected at higher temperatures. From this data two empirical linear equations for R_{bat} as a function of

temperature T (in K) can be derived:

$$R_{bat}(T) = 11.73\,\Omega - 0.038\,\frac{\Omega}{\mathrm{K}} \cdot T \quad \text{battery age} < 1 \text{ year} \tag{4–5}$$

$$R_{bat}(T) = 19.17\,\Omega - 0.064\,\frac{\Omega}{\mathrm{K}} \cdot T \quad \text{battery age} > 1 \text{ year} \tag{4–6}$$

Fortunately, Equation 4–5 for the undegraded battery is very close to the values measured on ground:

$$R_{bat}(T) = 11.93\,\Omega - 0.039\,\frac{\Omega}{\mathrm{K}} \cdot T \quad \text{measured on ground} \tag{4–7}$$

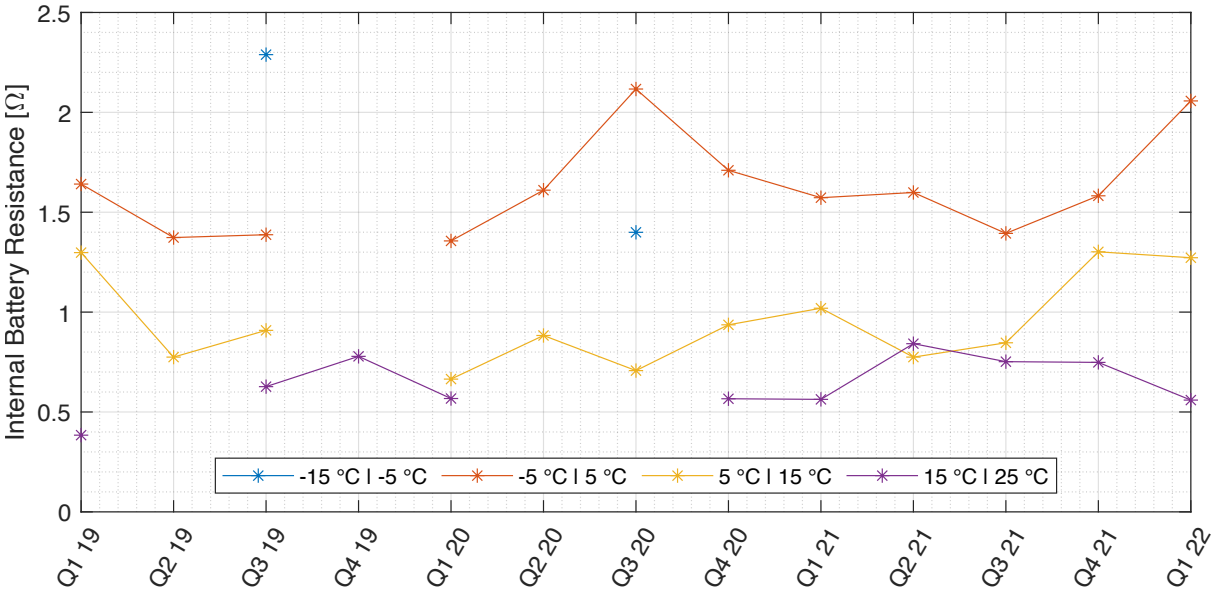

Fig. 4–5: Temperature Dependent Internal Battery Resistance Plotted over Time

A dependence on temperature can also be observed, when plotting R_{bat} over time on different temperature domains, as done in Figure 4–5. Here, broader temperature ranges of 10 °C had to be selected to avoid the formation of outliers due to a lack of data.
Particularly interesting is the fact that the first obtained resistance for temperatures of 15 °C to 25 °C coincides with the measurements on ground (0.42 Ω at room temperature [2]). This is to be expected, since the battery should still be in good condition shortly after startup, and shows that the analyses presented here are trustworthy. The existing simulation model of the battery, as part of the whole Simulink® model described before, was therefore updated to reflect the deviated resistance dependence from Equation 4–6, as the current status of the battery should be modeled by the digital twin.

4.2.1.2 Voltage Dependent

The same analyses as for temperature can be done for voltage ranges. As shown in Figure 4–6, the approximated OCV $U_{bat,OC}$ is in the range between 6.5 V and 8 V at

any given time. As stated before, the OCV can not be measured directly, instead the voltage readings depicted in Figure 4–6 were taken from voltage-current pairs with a magnitude of current $|I_{bat}|$ of smaller than 0.1 A.

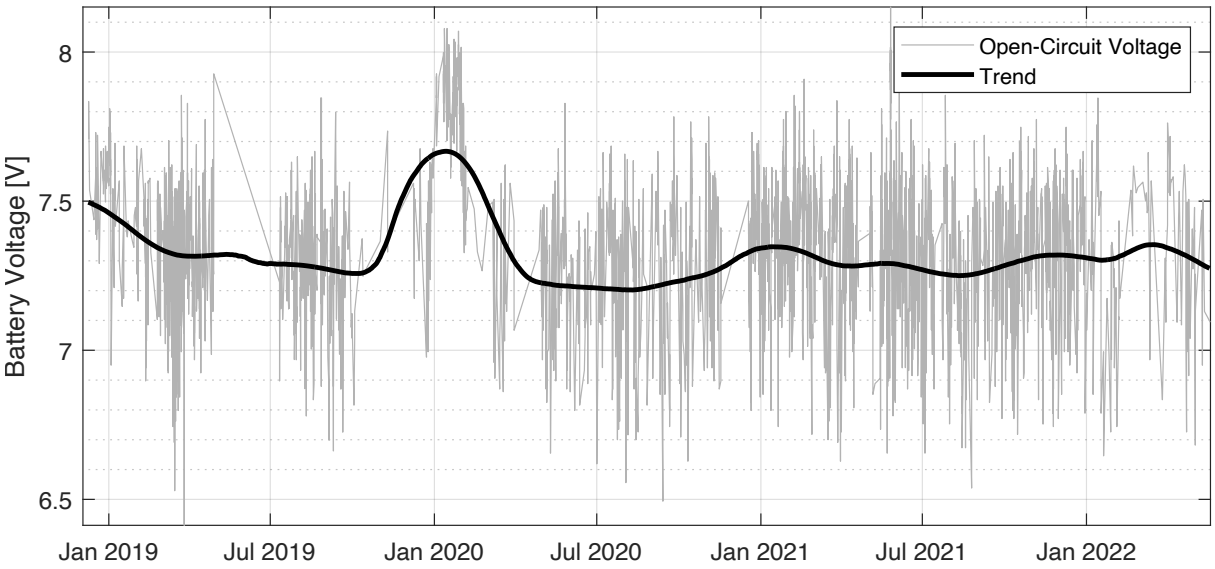

Fig. 4–6: Approximated Open-Circuit Voltage of the Battery with Trend

Only considering this selected set of voltage levels, but regarding current draws from 0.05 A to 0.5 A (typical range during satellite operations, while discharging the battery), gives us the following results for the DCIR as a function of battery voltage (see Figure 4–7).

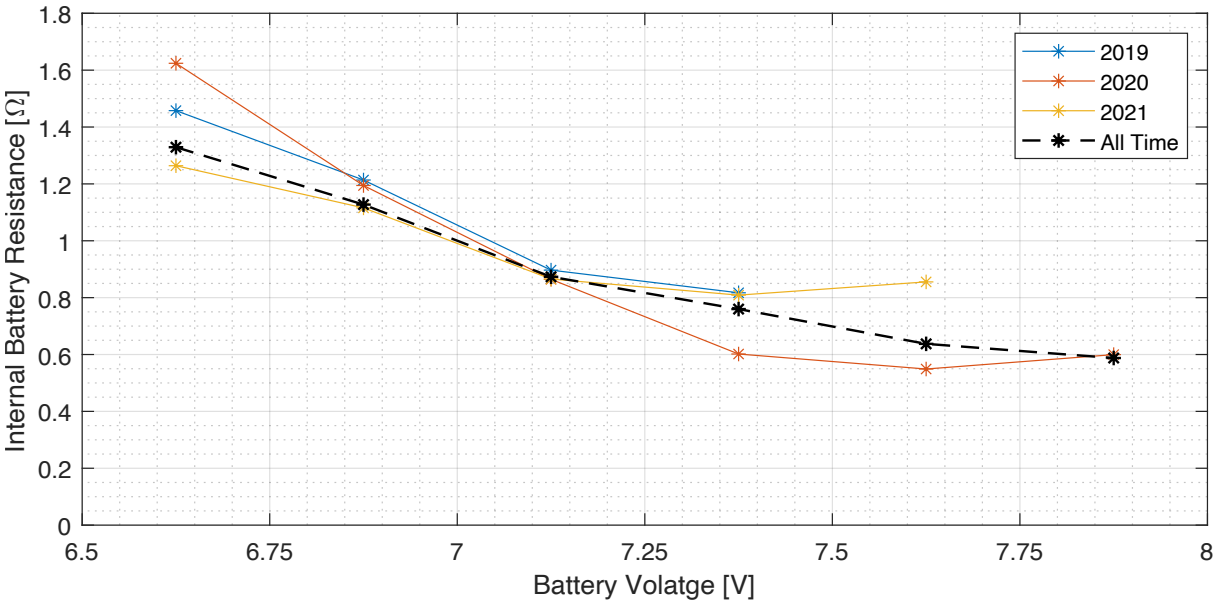

Fig. 4–7: Internal Battery Resistance Plotted over Voltage

As expected, the DCIR R_{bat} is inversely proportional to the battery's voltage U_{bat} and therefore also to the SOC. A detailed relationship between OCV and SOC of the battery installed in MOVE-II, which was obtained on ground, is shown in Table 4–1.

As illustrated in Figure 4–7 by the overlapping resistance curves, no consistent correlation of internal battery resistance and battery age could be observed, at least not in the lower voltage spectrum, where most of the data is located. This observation is supported by Figure 4–8, where no substantial trend in R_{bat} can be observed in any of the three voltage ranges. This implies that the increase in battery resistance over time, shown in Figure 4–3, is mainly caused by an increase in resistance at low temperatures as the battery ages.

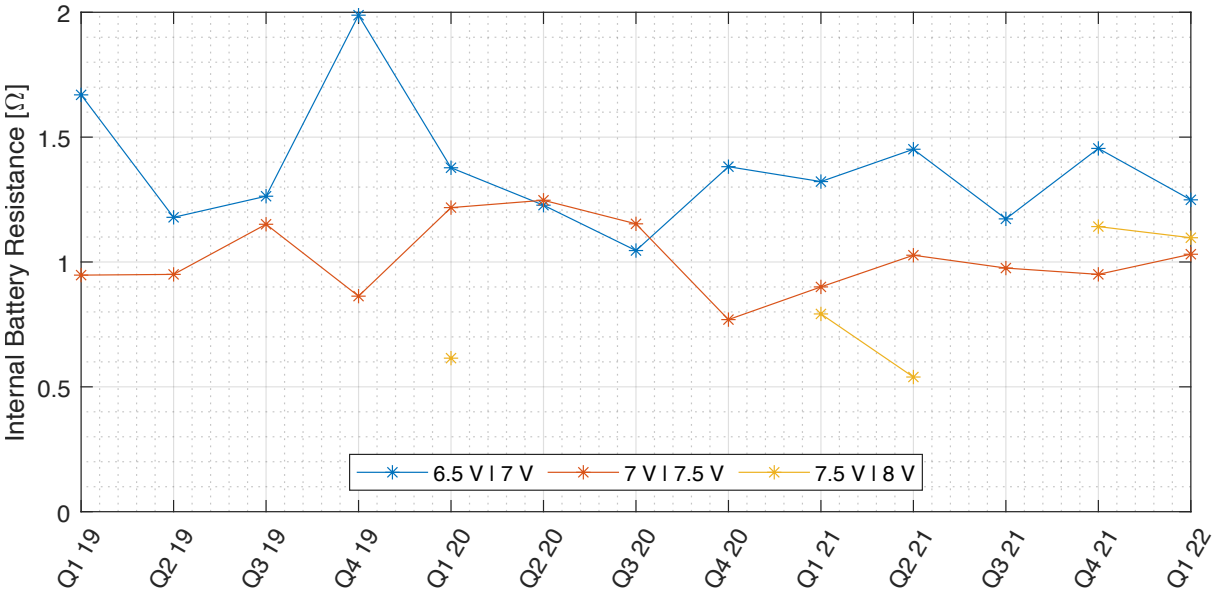

Fig. 4–8: Voltage Dependent Battery Resistance Plotted over Time

Form Figure 4–7 it seams like the relationship between voltage and internal battery resistance is linear from 6.5 V to 7.5 V and flattens out afterwards. A robust justification for this behavior still has to be found. However, when looking at the averaged resistance

Tab. 4–1: Relationship Between Open-Circuit Voltage and SOC of MOVE-II's Battery

Open-Circuit Voltage [V]	SOC [%]
6.50 - 6.75	2 - 4
6.75 - 7.00	4 - 7
7.00 - 7.25	7 - 11
7.25 - 7.50	11 - 37
7.50 - 7.75	37 - 67
7.75 - 8.00	67 - 84

from launch to April 2022 (all time), this dependence is less apparent. Here, R_{bat} can be approximated as a linear function of the battery voltage U_{bat}:

$$R_{bat}(U_{bat}) = 5.27\,\Omega - 0.60\,\frac{\Omega}{\mathrm{V}} \cdot U_{bat} \quad | \quad \forall\, U_{bat} \in [6.5, 8.0] \tag{4–8}$$

4.2.2 Simulink Verification Model

In order to validate the method of calculating the DCIR of MOVE-II's battery, described in subsection 3.1.2 and applied in subsection 4.2.1, a Simulink® model of the battery was used.
The model and the method of verification were described in chapter subsection 3.1.3. Essentially, a temperature dependant DCIR was modeled and should be recreated by performing the same calculations as on the orbit data. This means that only the voltage and current readings, which were modified to have a similar appearance as real satellite data, were taken into account.

As it turned out, the applied method of calculating the DCIR of the battery form orbit data exclusively, was able to determine the model's DCIR as a function of temperature with a confidence of 2.57 %. This is visually confirmed in Figure 4–9, as the calculated DCIR of the battery follows the modeled resistance closely. Thereby it is validated that the here used method to determine the DCIR of the battery onboard the satellite by the use of the orbit data is indeed precise.

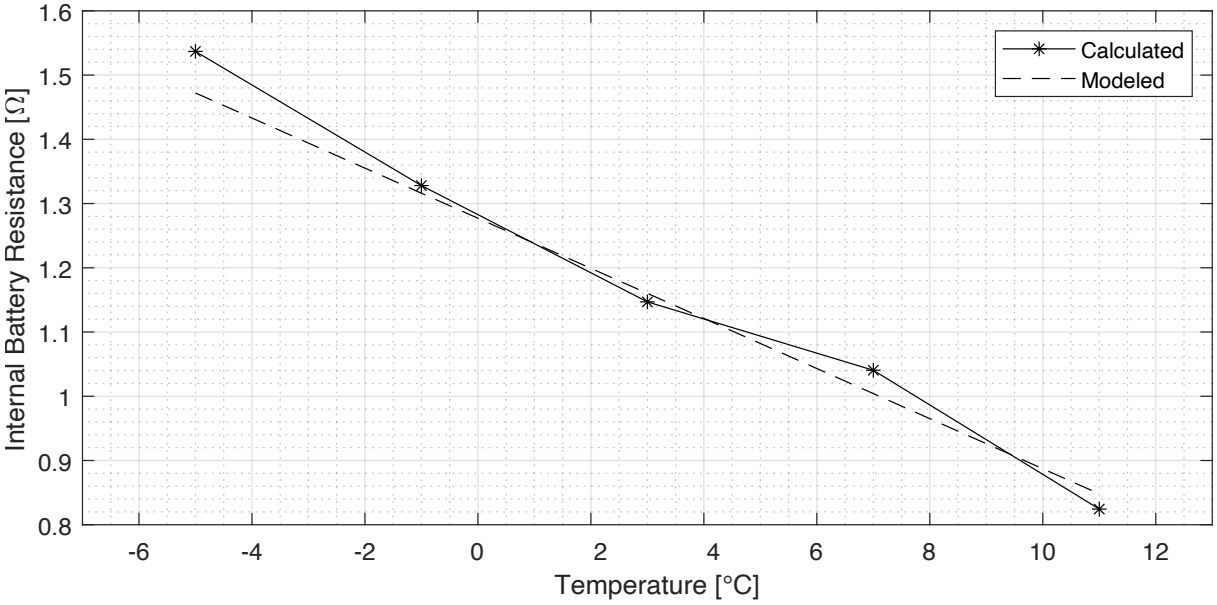

Fig. 4–9: Calculated Battery Resistance in Comparison to Modeled Battery Resistance

4.3 Uptime

The current uptime of the satellite's software (in seconds) is transmitted together with other orbit data. When MOVE-II is restarted, this counter is reset to zero. This allows

for a quantification of the stability of the operation, since operation times of more than one orbit period indicate that the satellite survives the eclipse phase without any reboot.

The recorded data is prepared according to the method described in subsection 3.1.4, by a combination of reducing and filtering the data. The values of the maximum uptimes that were recorded are plotted in Figure 4–10, together with a monthly mean of these.

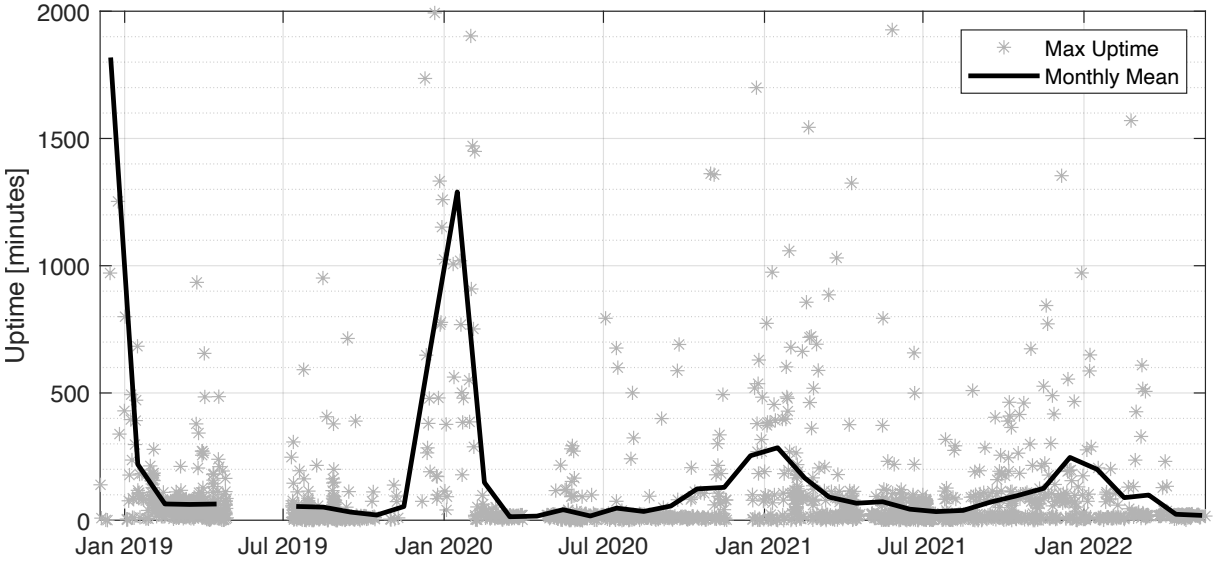

Fig. 4–10: Uptime of the Satellite's Software with Monthly Mean

The recorded uptimes go as high as 6783 min (70.5 orbits) on December 2018, right after launch. Afterwards, records in uptime were always seen in January: 4329 min (45 orbits) in 2020, 2034 min (21.2 orbits) in 2021 and 4726 min (49.1 orbits) in 2022. The higher value in 2022 than in 2021 could be caused by communication problems. The received data is known to be incomplete and thus can be missing values. Therefore it cannot be guaranteed that every maximum value corresponds to the actual one. More meaningful, however, is the mean value, which has continued to decrease over the years. This also points towards a significant reduction in battery capacity.

By comparing the uptime depicted here with the battery temperature (see Figure 4–1), it becomes apparent that in both cases local maxima coincide. This suggests that there is a correlation between temperature of the battery and the stability of the satellite's software. The reason for this being a reduced capacity of the battery at lower ambient temperatures, combined with higher electrical losses due to increased internal resistance, as proven in the previous section 4.2.
Ultimately, it can be seen that the satellite's stability varies greatly throughout the year. This is a rather surprising finding, as it was not clear that this is the case up to now.

5 Correlation of the Thermal Simulation Model

As stated before, the here correlated Thermal model was not developed for this paper exclusively. Instead, it is part of a much bigger Simulink® model, which is a result of many student research projects over the last few years and was for example described in [14].

The main goal here is to simulate the temperature of the battery as closely as possible to the telemetry data received from MOVE-II, in order to be able to model its behaviour more realistically. This is especially important since lithium-ion batteries are known to have significantly lower capacities at cold temperatures [25]. Therefore a realistic prediction of its temperature is especially important in terms of estimating the operational stability of the whole satellite.

5.1 Development of Correlation

Tuning the model is an iterative process. In order not to go beyond the scope of this work, some iterative steps that turned out to be unrewarding have been omitted here, providing a more targeted path to a well correlated simulation model.

5.1.1 Emissivity and Absorptivity Adaption of the Outer Sphere

It has been found in previous simulation runs that a variation of emissivity $\epsilon_{ext,IR}$ and absorptivity $\alpha_{ext,sol}$ of the outer sphere cause the greatest changes in the temperature profiles of the satellite. This is a logical consequence, as the ratio $\alpha_{sol}/\epsilon_{IR}$ of the satellites outside surface is a key parameter to control any satellite's temperature [16]. As MOVE-II's side and top panels are coated in matt white paint, a $\alpha_{sol}/\epsilon_{IR}$ ratio of 0.48 should be expected [4]. However, due to other surface materials used, as the solar cells for example ($\alpha_{sol}/\epsilon_{IR} \approx 0.7$), covering a large proportion of the satellite's surface, the average ratio is much higher. Therefore a $\alpha_{sol}/\epsilon_{IR}$ ratio of 1 with $\epsilon_{i,IR} = \alpha_{i,sol} = 0.7$ was chosen for the outer sphere and the Flappanels as an initial approximation.

At first, these parameters were altered with increments of 0.1 in both directions. The results are displayed in Figure 5–1, Table 5–1, and Table 5–2. The best results are highlighted in gray.

Tab. 5–1: RMSE of Data Set 21-08 with Variation of $\epsilon_{ext,IR}$ and $\alpha_{ext,sol}$ in a Step Size of 0.1

$\epsilon_{ext,IR}$ \ $\alpha_{ext,sol}$	0.6	0.7	0.8
0.6	12.3084 K	16.9351 K	21.4278 K
0.7	5.1993 K	9.5189 K	13.7627 K
0.8	1.7083 K	3.2532 K	7.2136 K

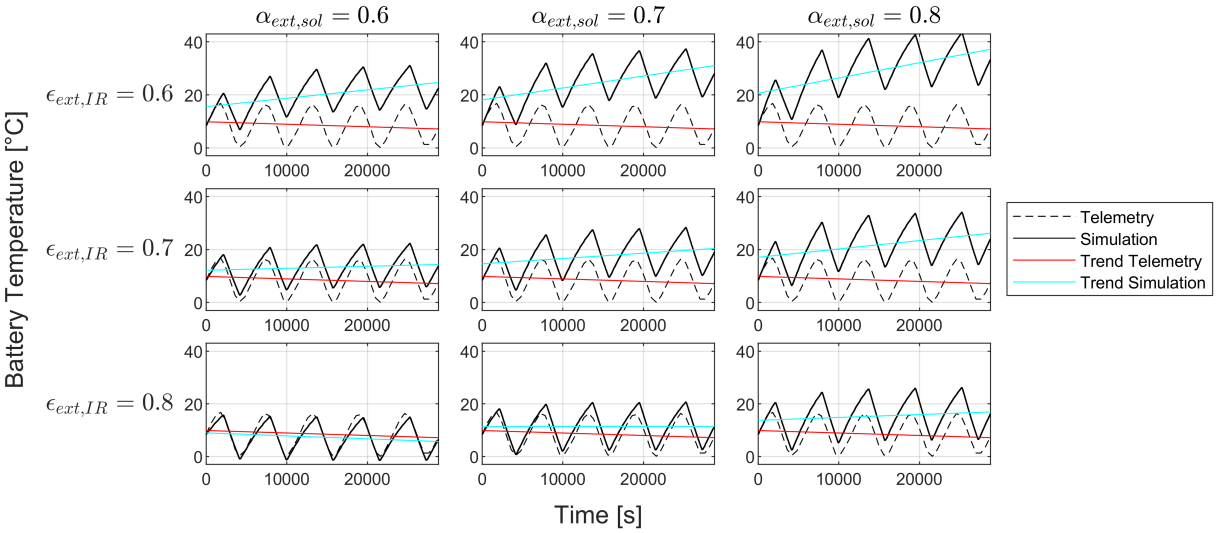

Fig. 5–1: Sweep of Parameters $\epsilon_{ext,IR}$ and $\alpha_{ext,sol}$ on Data Set 21-08 with a Step Size of 0.1

Tab. 5–2: Absolute Difference in Trend between Telemetry and Simulation of Data Set 21-08 with Variation of $\epsilon_{ext,IR}$ and $\alpha_{ext,sol}$ in a Step Size of 0.1

$\epsilon_{ext,IR}$ \ $\alpha_{ext,sol}$	0.6	0.7	0.8
0.6	$410.3876 \times 10^{-6}\ \frac{K}{s}$	$544.6053 \times 10^{-6}\ \frac{K}{s}$	$668.6757 \times 10^{-6}\ \frac{K}{s}$
0.7	$169.9769 \times 10^{-6}\ \frac{K}{s}$	$294.5002 \times 10^{-6}\ \frac{K}{s}$	$409.6226 \times 10^{-6}\ \frac{K}{s}$
0.8	$19.5664 \times 10^{-6}\ \frac{K}{s}$	$97.2336 \times 10^{-6}\ \frac{K}{s}$	$205.2309 \times 10^{-6}\ \frac{K}{s}$

It becomes apparent that the combination of $\epsilon_{ext,IR} = 0.8$ and $\alpha_{ext,sol} = 0.6$ is giving the best results, both in fit as well as in trend overlay. Therefore, further simulations with finer parameter increments are carried out in this value range. Figure 5–2 shows a simulation of data set 21-08 with $\epsilon_{ext,IR}$ in a range from 0.77 to 0.81 and $\alpha_{ext,sol}$ in a range from 0.58 to 0.62. The results in RMSE and trend are listed in Table 5–3 and 5–4.

Tab. 5–3: RMSE of Data Set 21-08 with Variation of $\epsilon_{ext,IR}$ and $\alpha_{ext,sol}$ in a Step Size of 0.02

$\epsilon_{ext,IR}$ \ $\alpha_{ext,sol}$	0.58	0.60	0.62
0.77	1.3776 K	1.5348 K	2.0798 K
0.79	1.8773 K	1.3912 K	1.3593 K
0.81	2.7894 K	2.0580 K	1.4765 K

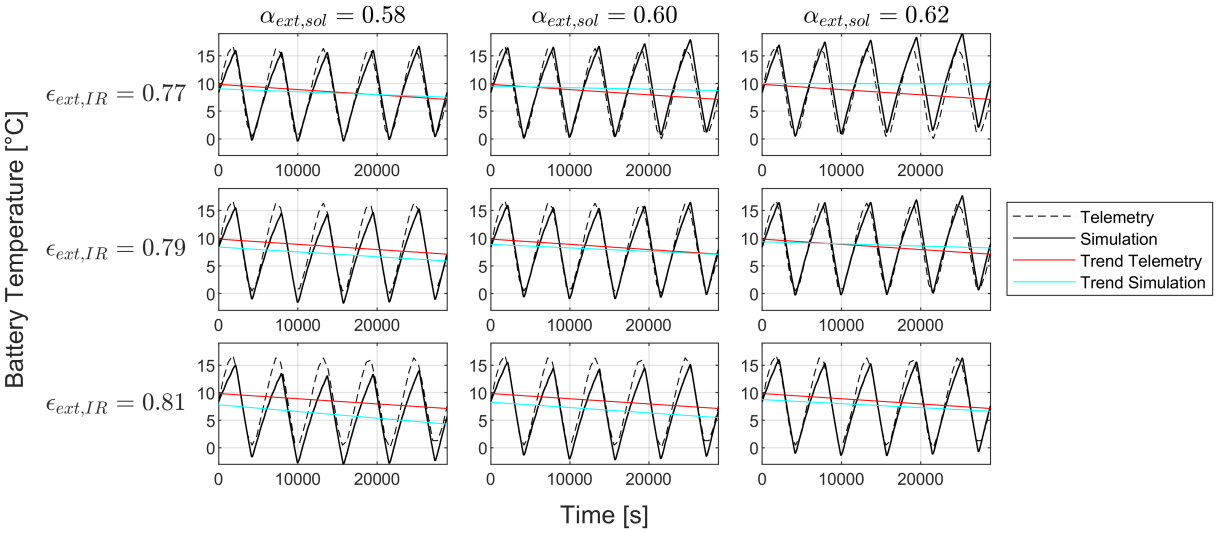

Fig. 5–2: Sweep of Parameters $\epsilon_{ext,IR}$ and $\alpha_{ext,sol}$ on Data Set 21-08 with a Step Size of 0.02

Tab. 5–4: Absolute Difference in Trend between Telemetry and Simulation of Data Set 21-08 with Variation of $\epsilon_{ext,IR}$ and $\alpha_{ext,sol}$ in a Step Size of 0.02

$\epsilon_{ext,IR}$ \ $\alpha_{ext,sol}$	0.58	0.60	0.62
0.77	$41.9705 \times 10^{-6}\ \frac{K}{s}$	$66.7767 \times 10^{-6}\ \frac{K}{s}$	$91.1775 \times 10^{-6}\ \frac{K}{s}$
0.79	$6.7960 \times 10^{-6}\ \frac{K}{s}$	$31.2972 \times 10^{-6}\ \frac{K}{s}$	$55.3975 \times 10^{-6}\ \frac{K}{s}$
0.81	$26.8720 \times 10^{-6}\ \frac{K}{s}$	$2.6631 \times 10^{-6}\ \frac{K}{s}$	$21.1491 \times 10^{-6}\ \frac{K}{s}$

From the results obtained, it can be seen that the smallest RMSE appears for $\epsilon_{ext,IR} = 0.79$ and $\alpha_{ext,sol} = 0.62$. The trend difference however is not the best, as it is achieved for $\epsilon_{ext,IR} = 0.81$ and $\alpha_{ext,sol} = 0.60$. However, as it can also be visually observed in Figure 5–2, there is an offset between simulation and telemetry data, which is also reflected in a significantly worse RMSE. The same accounts for the next best trend difference ($\epsilon_{ext,IR} = 0.79$; $\alpha_{ext,sol} = 0.58$). Considering both RMSE and difference in trend, the parameter set of $\epsilon_{ext,IR} = 0.79$ and $\alpha_{ext,sol} = 0.60$ is making a promising impression.

In order to further validate these findings, simulations were conducted with all data sets on the three best parameter combinations found above (see section A.3). The RMSE and trend values were then averaged and collected in Tables 5–5 and 5–6.

As observed in figure 5–3 and the corresponding tables 5–3 and 5–4, a small difference in trend is favorable, but in no way more important than a small RMSE. All trend values, listed in table 5–6 are relatively close to each other and in addition sufficiently small, with the greatest difference in trend being 228.3481×10^{-6} K/s, which is equal to 0.822 K/h. Combined with the fact that not all data sets have an equally uniform distribution of data points as 21-08, the calculated linear gradient can be misleading and

Tab. 5–5: Average RMSE Values on Yearly Basis – Calculated from Tables in Appendix A.3

$\alpha_{ext,sol}$	0.58	0.60	0.62
$\epsilon_{ext,IR}$	0.77	0.79	0.79
2019	2.1921 K	2.342 K	2.2748 K
2020	1.9926 K	2.1572 K	1.9300 K
2021	2.3064 K	2.3193 K	2.2095 K

Tab. 5–6: Average Difference in Trend on Yearly Basis – Calculated from Tables in Appendix A.3

$\alpha_{ext,sol}$	0.58	0.60	0.62
$\epsilon_{ext,IR}$	0.77	0.79	0.79
2019	$189.1132 \times 10^{-6}\ \frac{K}{s}$	$176.5781 \times 10^{-6}\ \frac{K}{s}$	$189.8000 \times 10^{-6}\ \frac{K}{s}$
2020	$215.2861 \times 10^{-6}\ \frac{K}{s}$	$202.7997 \times 10^{-6}\ \frac{K}{s}$	$228.3481 \times 10^{-6}\ \frac{K}{s}$
2021	$147.2729 \times 10^{-6}\ \frac{K}{s}$	$151.7483 \times 10^{-6}\ \frac{K}{s}$	$143.9357 \times 10^{-6}\ \frac{K}{s}$

is therefore not weighted as strongly as the RMSE. Thereby an interesting observation can be made: For the year 2019, an optimum in RMSE can be obtained with a combination of $\epsilon_{ext,IR} = 0.77$ and $\alpha_{ext,sol} = 0.58$, whereas for the years 2020 and 2021 the best RMSE is observed for simulations with $\epsilon_{ext,IR} = 0.79$ and $\alpha_{ext,sol} = 0.62$. This finding can have many causes, however, one of them should be highlighted here: In 2019, there were much fewer usable data sets than in subsequent years (see section A.2), which means that greater inaccuracies are to be expected.

5.1.2 Thermal Resistance Adaption Between Inner and Outer Sphere

According to Equation 3–7, thermal conductivity from the exterior node to the interior node is determined by the thermal resistance of eight aluminium carriers R_{al} and the thermal resistance of the solder mask R_{mask} connected in series:

$$R_{ext \to int} = R_{al} + R_{mask} \tag{5–1}$$

with

$$R_{al} = \frac{\frac{d_{ext,inner} - d_{int}}{2}}{\lambda_{al} \cdot A_{ext \to int,c}} \tag{5–2}$$

and

$$R_{mask} = \frac{h_{mask}}{\lambda_{mask} \cdot A_{ext \to int,c}} \tag{5–3}$$

The thickness of the mask h_{mask} is taken from [26]. With the initial parameters, given in Table A–1, R_{al} is calculated to 0.0448 W/K and R_{mask} is equal to 0.3125 W/K. This illustrates that the thermal resistance of the solder mask has a much greater impact

on the conductive heat flow than the well conducting aluminium, as the ratio R_{mask}/R_{al} is almost 7. Therefore, only the thermal conductivity of the solder mask λ_{mask} will be varied, in order to influence the conductive heat flow from the external to the internal node.
The second way of heat transfer between the nodes is through radiation ($\dot{Q}_{ext\rightarrow int,r}$ in Equation 3–6). The limiting factor here being the emissivities of the interior surface, as well as the inner side of the exterior sphere, which is assumed to be the same as $\epsilon_{ext,IR}$ of its outward facing surface. As $\epsilon_{ext,IR}$ is allready well tuned, only $\epsilon_{int,IR}$ will be modified here.

The initial values of $\epsilon_{int,IR}$ and λ_{mask} are changed up and down by 0.1, respectively, in the first step. The results of the conducted simulations are shown in Figure 5–3 as well as Tables 5–7 and 5–8.

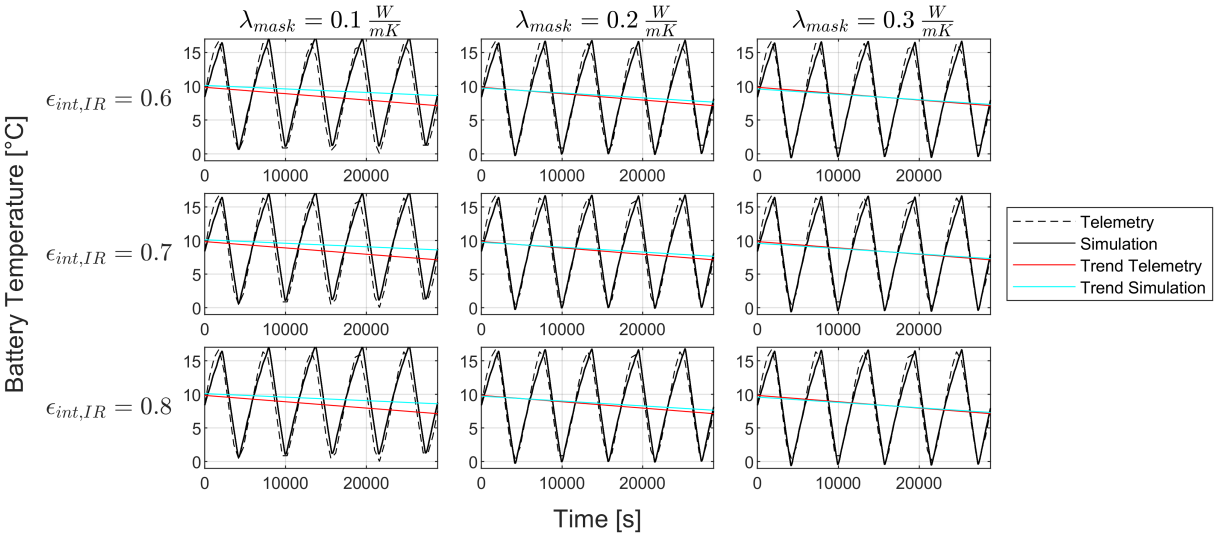

Fig. 5–3: Sweep of Parameters $\epsilon_{int,IR}$ and λ_{mask} on Data Set 21-08 with a Step Size of 0.1

Tab. 5–7: RMSE of Data Set 21-08 with Variation of $\epsilon_{int,IR}$ and λ_{mask} in a Step Size of 0.1

$\epsilon_{int,IR}$ \ λ_{mask}	0.1 $\frac{W}{mK}$	0.2 $\frac{W}{mK}$	0.3 $\frac{W}{mK}$
0.6	1.7158 K	1.2542 K	1.1614 K
0.7	1.7081 K	1.2528 K	1.1610 K
0.8	1.7008 K	1.2514 K	1.1606 K

Tab. 5–8: Absolute Difference in Trend between Telemetry and Simulation of Data Set 21-08 with Variation of $\epsilon_{int,IR}$ and λ_{mask} in a Step Size of 0.1

$\epsilon_{int,IR}$ \ λ_{mask}	0.1 $\frac{\mathrm{W}}{\mathrm{m\,K}}$	0.2 $\frac{\mathrm{W}}{\mathrm{m\,K}}$	0.3 $\frac{\mathrm{W}}{\mathrm{m\,K}}$
0.6	$42.2452 \times 10^{-6}\ \frac{\mathrm{K}}{\mathrm{s}}$	$21.8595 \times 10^{-6}\ \frac{\mathrm{K}}{\mathrm{s}}$	$15.0188 \times 10^{-6}\ \frac{\mathrm{K}}{\mathrm{s}}$
0.7	$41.9567 \times 10^{-6}\ \frac{\mathrm{K}}{\mathrm{s}}$	$21.7759 \times 10^{-6}\ \frac{\mathrm{K}}{\mathrm{s}}$	$14.9766 \times 10^{-6}\ \frac{\mathrm{K}}{\mathrm{s}}$
0.8	$41.6813 \times 10^{-6}\ \frac{\mathrm{K}}{\mathrm{s}}$	$21.6956 \times 10^{-6}\ \frac{\mathrm{K}}{\mathrm{s}}$	$14.9360 \times 10^{-6}\ \frac{\mathrm{K}}{\mathrm{s}}$

While analyzing Tables 5–7 and 5–8 it becomes apparent that the alteration of $\epsilon_{int,IR}$ is not resulting in great effects on the RMSE or the difference in trend. The increase in λ_{mask}, however, results in both smaller RMSE and a smaller difference in trend. In order to visualize this difference in a more descriptive way, an overlay of simulations with different λ_{mask} values and $\epsilon_{int,IR} = 0.7$ is presented in Figure 5–4 over the period of one orbit.

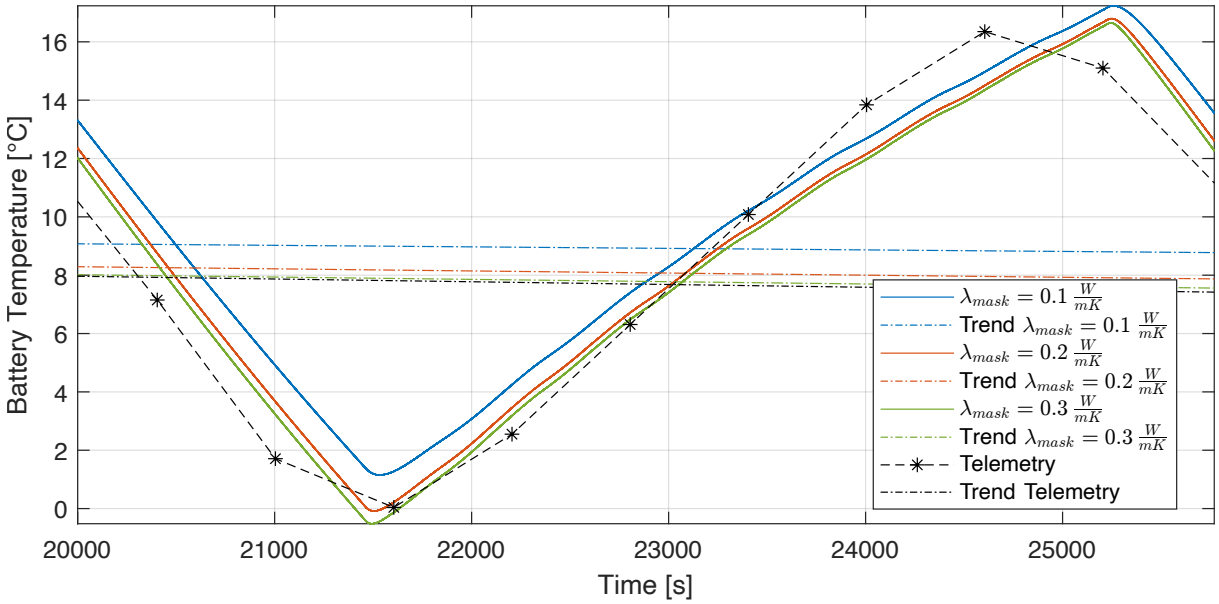

Fig. 5–4: Sweep of λ_{mask} on Data Set 21-08 with $\epsilon_{int,IR} = 0.7$

The simulation with a very small thermal conductivity of the solder mask λ_{mask} clearly shows higher temperatures of the internal node, thus resulting in lower RMSEs. The difference in temperature between $\lambda_{mask} = 0.2\,\mathrm{W/(m\,K)}$ and $\lambda_{mask} = 0.3\,\mathrm{W/(m\,K)}$, however, is rather small. Moreover, no temperature shift can be observed in the time domain.
By simulating even higher thermal conductivities λ_{mask} (see Tables 5–9 and 5–10), a further reduction of the RMSE can be observed. However, the difference between these is becoming increasingly smaller, indicating a convergence and making a visualization of the results pointless.

Tab. 5–9: RMSE of Data Set 21-08 with Variation of $\epsilon_{int,IR}$ and λ_{mask} in a Step Size of 0.1

$\epsilon_{int,IR}$ \ λ_{mask}	0.4 $\frac{\mathrm{W}}{\mathrm{m\,K}}$	0.5 $\frac{\mathrm{W}}{\mathrm{m\,K}}$	0.6 $\frac{\mathrm{W}}{\mathrm{m\,K}}$
0.6	1.1340 K	1.1246 K	1.1214 K
0.7	1.1338 K	1.1245 K	1.1214 K
0.8	1.1337 K	1.1245 K	1.1214 K

Tab. 5–10: Absolute Difference in Trend between Telemetry and Simulation of Data Set 21-08 with Variation of $\epsilon_{int,IR}$ and λ_{mask} in a Step Size of 0.1

$\epsilon_{int,IR}$ \ λ_{mask}	0.4 $\frac{\mathrm{W}}{\mathrm{m\,K}}$	0.5 $\frac{\mathrm{W}}{\mathrm{m\,K}}$	0.6 $\frac{\mathrm{W}}{\mathrm{m\,K}}$
0.6	$11.5908 \times 10^{-6}\ \frac{\mathrm{K}}{\mathrm{s}}$	$9.5316 \times 10^{-6}\ \frac{\mathrm{K}}{\mathrm{s}}$	$8.1579 \times 10^{-6}\ \frac{\mathrm{K}}{\mathrm{s}}$
0.7	$11.5641 \times 10^{-6}\ \frac{\mathrm{K}}{\mathrm{s}}$	$9.5125 \times 10^{-6}\ \frac{\mathrm{K}}{\mathrm{s}}$	$8.1432 \times 10^{-6}\ \frac{\mathrm{K}}{\mathrm{s}}$
0.8	$11.5383 \times 10^{-6}\ \frac{\mathrm{K}}{\mathrm{s}}$	$9.4941 \times 10^{-6}\ \frac{\mathrm{K}}{\mathrm{s}}$	$8.1290 \times 10^{-6}\ \frac{\mathrm{K}}{\mathrm{s}}$

To avoid unreasonably high values and overfitting, a preliminary improved value of $\lambda_{mask} = 0.3\,\mathrm{W/(m\,K)}$ is assumed. Since the change in emissivity of the internal sphere did not produce significant results, it remains unchanged at $\epsilon_{int,IR} = 0.7$.

In the next step, this change in λ_{mask} is verified by simulations based on other data sets. For this purpose the values highlighted in Table 5–5 serve as a baseline with the initial value of λ_{mask} being $0.2\,\mathrm{W/(m\,K)}$. The results of this comparison can be seen in Tables 5–11 and 5–12. It becomes apparent that other than slightly lower differences in trend, the average RMSE is elevated, meaning an increase in conductivity of the solder mask λ_{mask} results in overall worse fit. Data sets from 2019 are making an exception here, but since the difference is very small and the average is only calculated from four values, thus containing more uncertainty, the slight improvement is being ignored here.

Tab. 5–11: Average RMSE Values on Yearly Basis – Calculated from Tables in Appendix A.3

λ_{mask}	0.2 $\frac{\mathrm{W}}{\mathrm{m\,K}}$	0.3 $\frac{\mathrm{W}}{\mathrm{m\,K}}$
2019 ($\frac{\alpha_{ext,sol}}{\epsilon_{ext,IR}} = \frac{0.58}{0.77}$)	2.1921 K	2.1705 K
2020 ($\frac{\alpha_{ext,sol}}{\epsilon_{ext,IR}} = \frac{0.62}{0.79}$)	1.9300 K	1.9732 K
2021 ($\frac{\alpha_{ext,sol}}{\epsilon_{ext,IR}} = \frac{0.62}{0.79}$)	2.2095 K	2.2624 K

Tab. 5–12: Average Difference in Trend on Yearly Basis – Calculated from Tables in Appendix A.3

λ_{mask}	0.2 $\frac{W}{mK}$	0.3 $\frac{W}{mK}$
2019 ($\frac{\alpha_{ext,sol}}{\epsilon_{ext,IR}} = \frac{0.58}{0.77}$)	189.1132 $\times$ 10^{-6} $\frac{K}{s}$	176.7047 $\times$ 10^{-6} $\frac{K}{s}$
2020 ($\frac{\alpha_{ext,sol}}{\epsilon_{ext,IR}} = \frac{0.62}{0.79}$)	228.3481 $\times$ 10^{-6} $\frac{K}{s}$	215.0590 $\times$ 10^{-6} $\frac{K}{s}$
2021 ($\frac{\alpha_{ext,sol}}{\epsilon_{ext,IR}} = \frac{0.62}{0.79}$)	143.9357 $\times$ 10^{-6} $\frac{K}{s}$	142.5961 $\times$ 10^{-6} $\frac{K}{s}$

In summary, a significant improvement in fit of the simulation can not be detected. Neither by altering the conductivity of the solder mask λ_{mask}, influencing the conductive heat transfer, nor by changing the emissivity of the internal sphere $\epsilon_{int,IR}$, which is the main influencing factor for radiative heat transfer.

5.1.3 Thermal Capacitance Adaption

In order to model transient thermal behaviours of the battery, also the thermal capacities of the nodes need to be looked at in more detail. To get a first feel for the impact of these parameters, nine different simulations with an alteration of the specific thermal capacity of the internal node $c_{p,int}$ and the external node $c_{p,ext}$ were conducted with very large variations of $\pm$200 J/(kg K). The initial values for $c_{p,int}$ and $c_{p,ext}$ prior to alteration were: $c_{p,int}$ = 994.89 J/(kg K) and $c_{p,ext}$ = 687 J/(kg K). The results are depicted in Figure 5–5, as well as Tables 5–13 and 5–14.

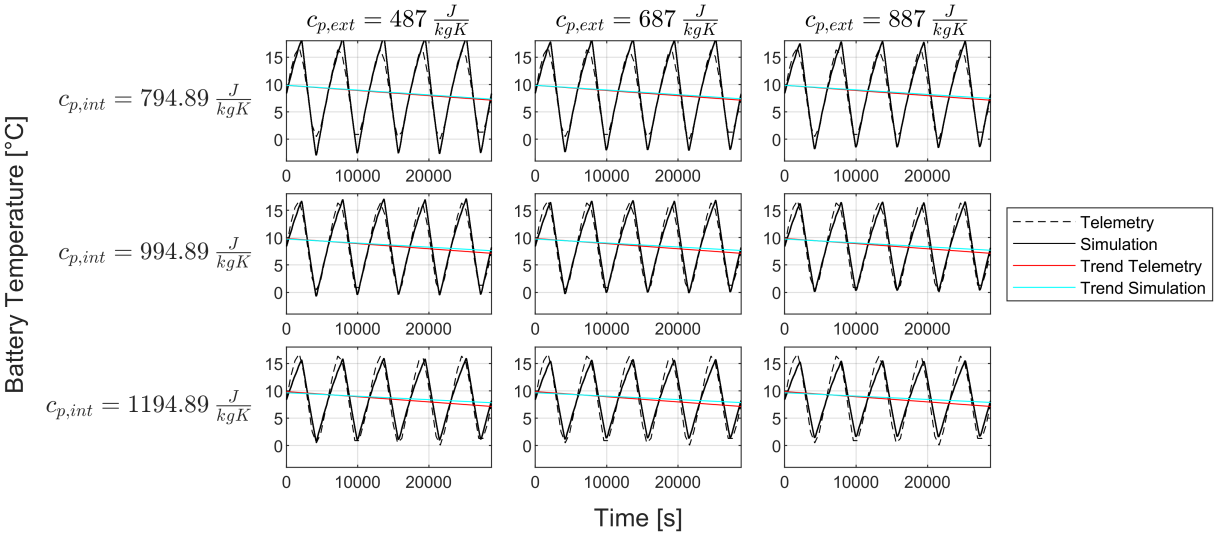

Fig. 5–5: Sweep of Parameters $c_{p,int}$ and $c_{p,ext}$ on Data Set 21-08 with a Step Size of 200 J/(kg K)

Tab. 5–13: RMSE of Data Set 21-08 with Variation of $c_{p,int}$ and $c_{p,ext}$ in a Step Size of 200 J/(kg K)

$c_{p,int}$ \ $c_{p,ext}$	487 $\frac{\text{J}}{\text{kg K}}$	687 $\frac{\text{J}}{\text{kg K}}$	887 $\frac{\text{J}}{\text{kg K}}$
794.89 $\frac{\text{J}}{\text{kg K}}$	1.3678 K	1.2609 K	1.2106 K
994.89 $\frac{\text{J}}{\text{kg K}}$	1.1562 K	1.2528 K	1.3610 K
1194.89 $\frac{\text{J}}{\text{kg K}}$	1.5552 K	1.6766 K	1.7940 K

Tab. 5–14: Absolute Difference in Trend between Telemetry and Simulation of Data Set 21-08 with Variation of $c_{p,int}$ and $c_{p,ext}$ in a Step Size of 200 J/(kg K)

$c_{p,int}$ \ $c_{p,ext}$	487 $\frac{\text{J}}{\text{kg K}}$	687 $\frac{\text{J}}{\text{kg K}}$	887 $\frac{\text{J}}{\text{kg K}}$
794.89 $\frac{\text{J}}{\text{kg K}}$	$6.1263 \times 10^{-6}\ \frac{\text{K}}{\text{s}}$	$8.4810 \times 10^{-6}\ \frac{\text{K}}{\text{s}}$	$10.6769 \times 10^{-6}\ \frac{\text{K}}{\text{s}}$
994.89 $\frac{\text{J}}{\text{kg K}}$	$20.1898 \times 10^{-6}\ \frac{\text{K}}{\text{s}}$	$21.7759 \times 10^{-6}\ \frac{\text{K}}{\text{s}}$	$23.2789 \times 10^{-6}\ \frac{\text{K}}{\text{s}}$
1194.89 $\frac{\text{J}}{\text{kg K}}$	$30.7534 \times 10^{-6}\ \frac{\text{K}}{\text{s}}$	$31.8820 \times 10^{-6}\ \frac{\text{K}}{\text{s}}$	$32.9647 \times 10^{-6}\ \frac{\text{K}}{\text{s}}$

In fact a smaller RMSE can be obtained for a simulation with lower thermal capacity of the outer sphere. By taking a closer look at five of the results in Figure 5–6 and Figure 5–7 (orange is the same simulation in both figures) it becomes apparent that both the change in specific thermal capacity of the internal node $c_{p,int}$, as well as the change in $c_{p,ext}$ of the external node result in an inversely proportional change of the internal node's temperature gradient and therefore a change in the maximum and minimum temperatures seen. Thereby a difference in $c_{p,int}$ has a greater impact than a variation of $c_{p,ext}$. This also explains, why a reduction of $c_{p,ext}$ is able to produce a better RMSE than an equivalent reduction in $c_{p,int}$, as the battery temperature is more sensitive to changes of $c_{p,int}$ and therefore overshoots its best fit. In order to prove this theory, more simulations with specific capacities of the internal node $c_{p,int}$, ranging from 794.89 J/(kg K) to 994.89 J/(kg K) in increments of 50 J/(kg K) with $c_{p,ext} = 687$ J/(kg K), were conducted. The results are shown in Figure 5–8, as well as Tables 5–15 and 5–16.

Tab. 5–15: RMSE of Data Set 21-08 with Reduction of $c_{p,int}$ in a Step Size of 50 J K/kg

$c_{p,int}$ \ $c_{p,ext}$	687 $\frac{\text{J}}{\text{kg K}}$
794.89 $\frac{\text{J}}{\text{kg K}}$	1.2609 K
844.89 $\frac{\text{J}}{\text{kg K}}$	1.1709 K
894.89 $\frac{\text{J}}{\text{kg K}}$	1.1492 K
944.89 $\frac{\text{J}}{\text{kg K}}$	1.1821 K
994.89 $\frac{\text{J}}{\text{kg K}}$	1.2528 K

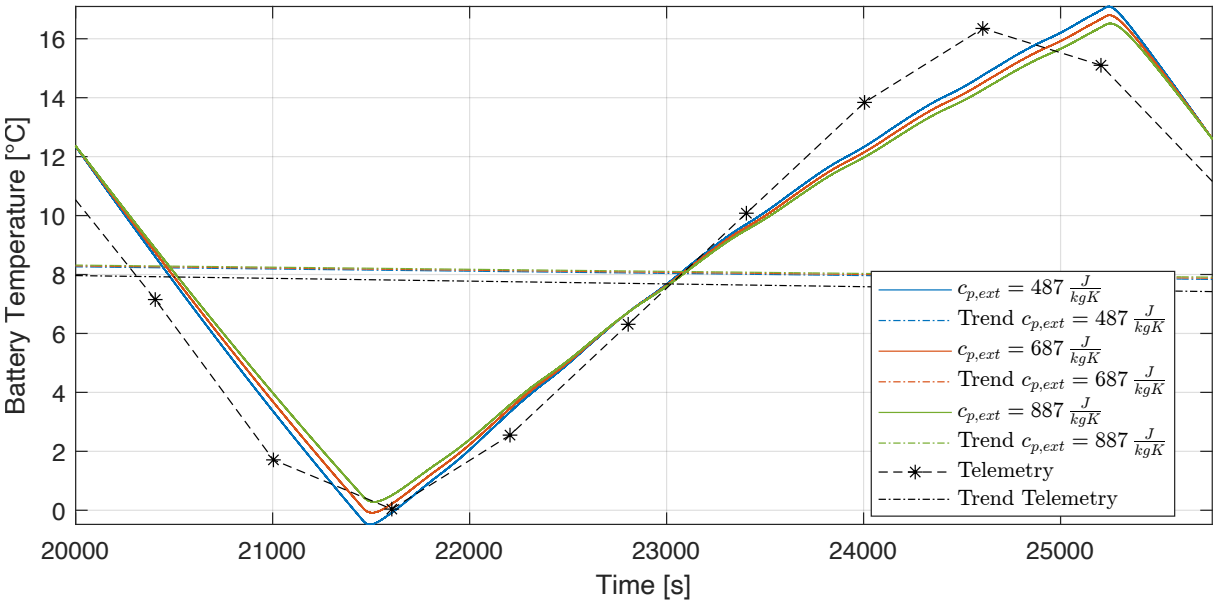

Fig. 5–6: Sweep of $c_{p,ext}$ on Data Set 21-08 with $c_{p,int} = 994.89\,\mathrm{J\,K/kg}$

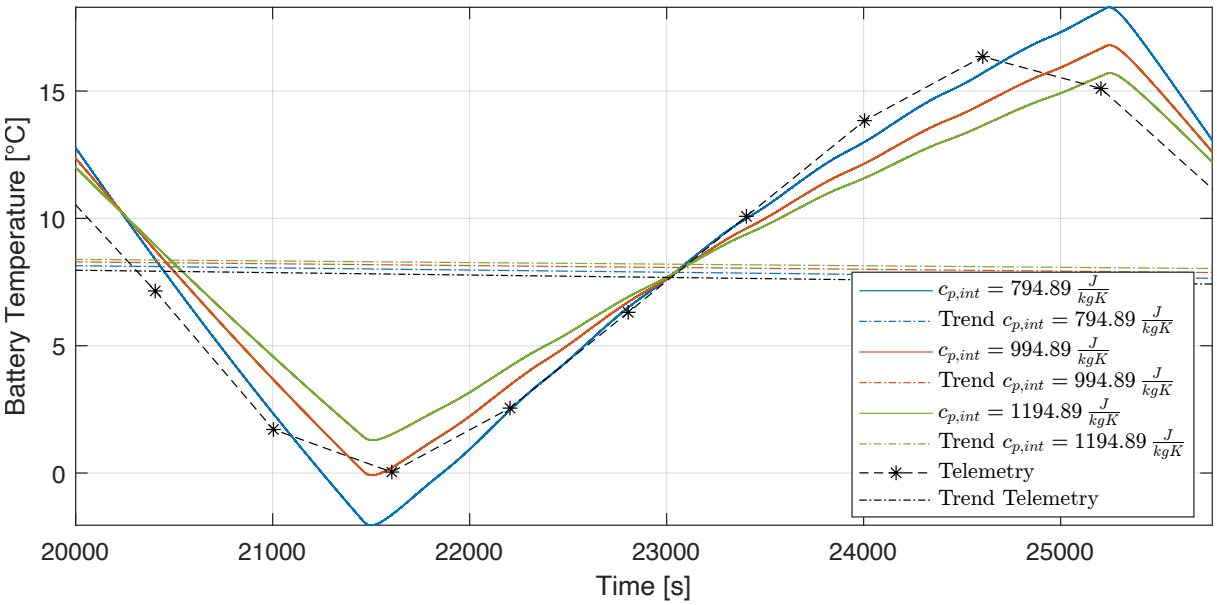

Fig. 5–7: Sweep of $c_{p,int}$ on Data Set 21-08 with $c_{p,ext} = 687\,\mathrm{J\,K/kg}$

Tab. 5–16: Absolute Difference in Trend between Telemetry and Simulation of Data Set 21-08 with Reduction of $c_{p,int}$ in a Step Size of 50 J K/kg

$c_{p,int}$ \ $c_{p,ext}$	$687 \frac{\mathrm{J}}{\mathrm{kg\,K}}$
$794.89 \frac{\mathrm{J}}{\mathrm{kg\,K}}$	$8.4810 \times 10^{-6} \frac{\mathrm{K}}{\mathrm{s}}$
$844.89 \frac{\mathrm{J}}{\mathrm{kg\,K}}$	$12.1921 \times 10^{-6} \frac{\mathrm{K}}{\mathrm{s}}$
$894.89 \frac{\mathrm{J}}{\mathrm{kg\,K}}$	$15.6237 \times 10^{-6} \frac{\mathrm{K}}{\mathrm{s}}$
$944.89 \frac{\mathrm{J}}{\mathrm{kg\,K}}$	$18.8089 \times 10^{-6} \frac{\mathrm{K}}{\mathrm{s}}$
$994.89 \frac{\mathrm{J}}{\mathrm{kg\,K}}$	$21.7759 \times 10^{-6} \frac{\mathrm{K}}{\mathrm{s}}$

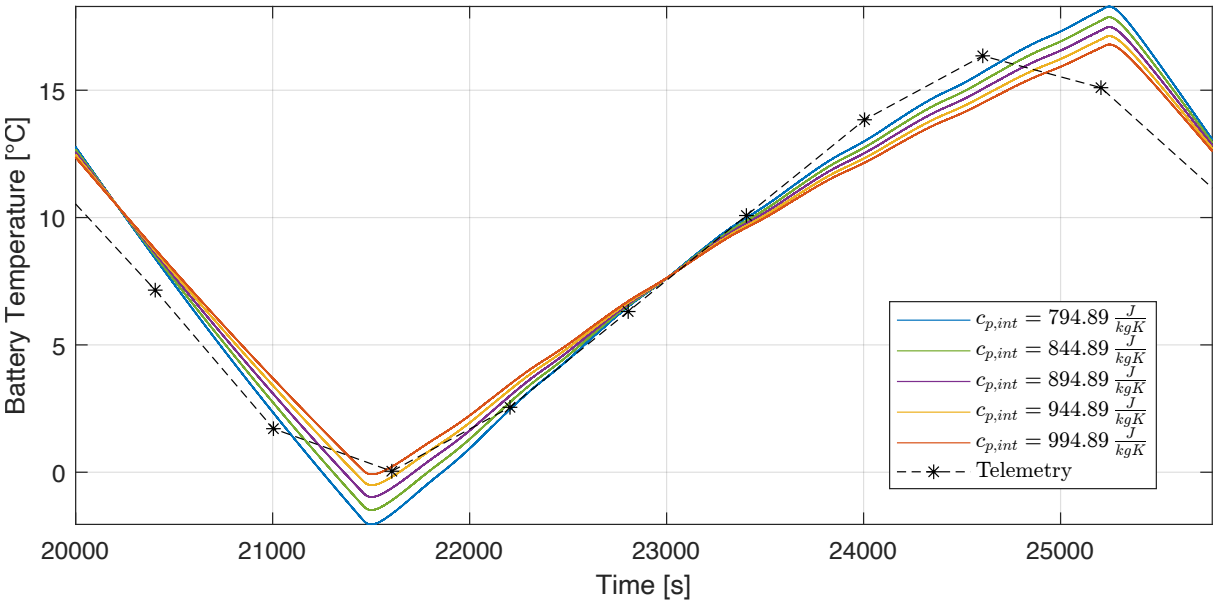

Fig. 5–8: Sweep of $c_{p,int}$ on Data Set 21-08 with $c_{p,ext} = 687$ J K/kg with Step Size of 50 J K/kg

This does prove that a change in $c_{p,int}$ is also very capable of reducing the RMSE to an improved value and that a change to 794.89 J/(kg K) is just too extreme. Because the fit of the simulation with reduced internal thermal capacity is even better than the one with lower external thermal capacity, an improved parameter set with $c_{p,int} = 894.89$ J/(kg K) and $c_{p,ext} = 687$ J/(kg K) is assumed.
To verify these new parameters, further simulations are conducted on more data sets with the updated model. The results can be found in Tables 5–17 and 5–18. This shows that on average a decrease in internal capacity $c_{p,int}$ from 994.89 J/(kg K) to 894.89 J/(kg K) does not result in lower RMSE values. Although the difference in trend does get smaller, the increase in RMSE weighs heavier due to reasons mentioned in subsection 3.2.4.

Tab. 5–17: Comparison of Average RMSE Values on Yearly Basis with Alteration of $c_{p,int}$ – Calculated from Tables in Appendix A.3

$c_{p,ext}$	687 $\frac{\text{J}}{\text{kg K}}$	
$c_{p,int}$	994.89 $\frac{\text{J}}{\text{kg K}}$	894.89 $\frac{\text{J}}{\text{kg K}}$
2019 ($\frac{\alpha_{ext,sol}}{\epsilon_{ext,IR}} = \frac{0.58}{0.77}$)	2.1921 K	2.2029 K
2020 ($\frac{\alpha_{ext,sol}}{\epsilon_{ext,IR}} = \frac{0.62}{0.79}$)	1.9300 K	2.0670 K
2021 ($\frac{\alpha_{ext,sol}}{\epsilon_{ext,IR}} = \frac{0.62}{0.79}$)	2.2095 K	2.2902 K

Tab. 5–18: Comparison of Average Difference in Trend on Yearly Basis with Alteration of $c_{p,int}$ – Calculated from Tables in Appendix A.3

$c_{p,ext}$	687 $\frac{\mathrm{J}}{\mathrm{kg\,K}}$	
$c_{p,int}$	994.89 $\frac{\mathrm{J}}{\mathrm{kg\,K}}$	894.89 $\frac{\mathrm{J}}{\mathrm{kg\,K}}$
2019 ($\frac{\alpha_{ext,sol}}{\epsilon_{ext,IR}} = \frac{0.58}{0.77}$)	189.1132 $\times 10^{-6}$ $\frac{\mathrm{K}}{\mathrm{s}}$	158.4792 $\times 10^{-6}$ $\frac{\mathrm{K}}{\mathrm{s}}$
2020 ($\frac{\alpha_{ext,sol}}{\epsilon_{ext,IR}} = \frac{0.62}{0.79}$)	228.348 11 $\times 10^{-6}$ $\frac{\mathrm{K}}{\mathrm{s}}$	214.9122 $\times 10^{-6}$ $\frac{\mathrm{K}}{\mathrm{s}}$
2021 ($\frac{\alpha_{ext,sol}}{\epsilon_{ext,IR}} = \frac{0.62}{0.79}$)	143.9357 $\times 10^{-6}$ $\frac{\mathrm{K}}{\mathrm{s}}$	137.4720 $\times 10^{-6}$ $\frac{\mathrm{K}}{\mathrm{s}}$

After all, no improvement in the overall fit by means of RMSE could be observed by altering the thermal capacitance of the inner $c_{p,int}$ nor the outer shell $c_{p,ext}$. Therefore no parameter adjustment is being performed here.

5.2 Results

One could think of many other adjustments to the parameters, influencing the models behaviour but since the results of the simulation are already satisfactory this would go beyond the scope of this term paper, so the attempt of improvement (conducted in the previous section 5.1) ends here.

In summary, a significant improvement in the accuracy of the simulation could only be obtained by adapting the emissivity $\epsilon_{ext,IR}$ and absorptivity $\alpha_{ext,sol}$ of the outer node. A further change in thermal resistance between the internal and external node, as well as a variation in thermal capacity did not result in improved predictions of the satellites battery temperature by the simulation.

An exemplary comparison based on data set 21-08 between the uncorrelated and the correlated Simulink® model can be seen in Figure 5–9. Due to an originally overestimated ratio between absorptivity and emissivity ($\alpha_{ext,sol}/\epsilon_{ext,IR} = 0.7/0.7$) of 1.0, the settled temperature of the battery in the uncorrelated model is hotter than the telemetry data shows. This is emphasized by a high RMSE of 9.5189 K. By reducing the ratio $\alpha_{ext,sol}/\epsilon_{ext,IR} = 0.62/0.79$ to 0.7848 for data sets starting at the beginning of 2020, a decreased RMSE by a factor of 7 to 1.3593 K could be observed for the particular data set 21-08. Furthermore it was found that for data sets form 2019 (the year after launch of MOVE-II), a reduced $\alpha_{ext,sol}$ to $\epsilon_{ext,IR}$ ratio of $0.58/0.77 = 0.7532$ ensured better correlation results. With these tuned parameters (collected in Table A–2), an RMSE of 2.0973 K, averaged over all data sets, was achieved. A collection of comparisons between correlated and uncorrelated simulation model over the years with regard to the telemetry data can be found in Figure 5–10.

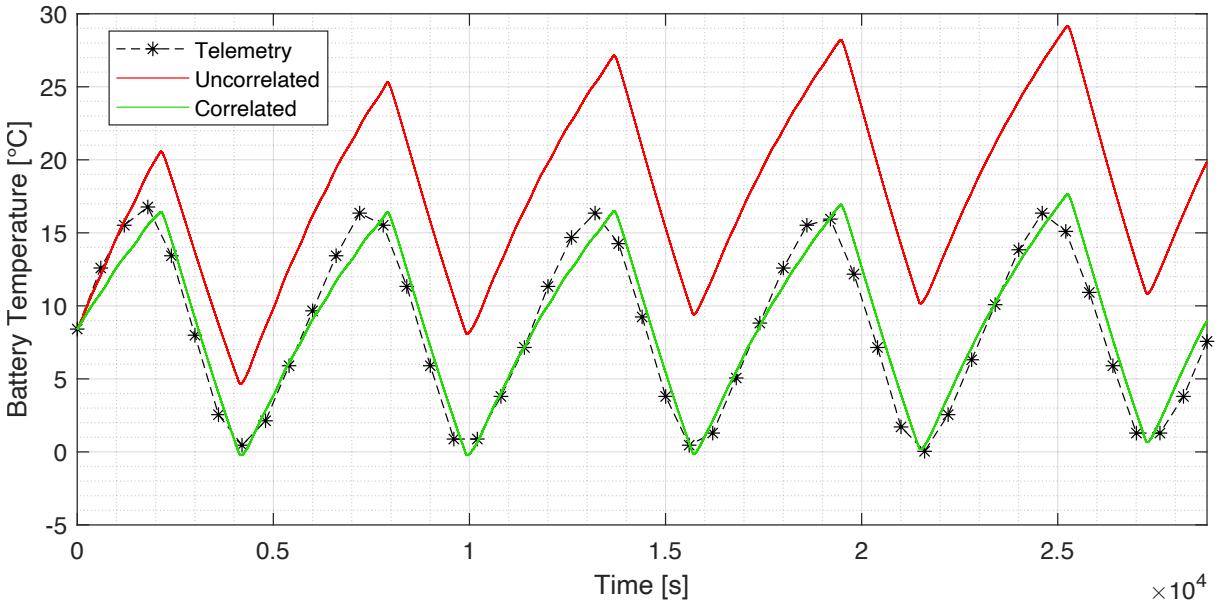

Fig. 5–9: Comparison of Uncorrelated and Correlated Simulink® Model on Data Set 21-08

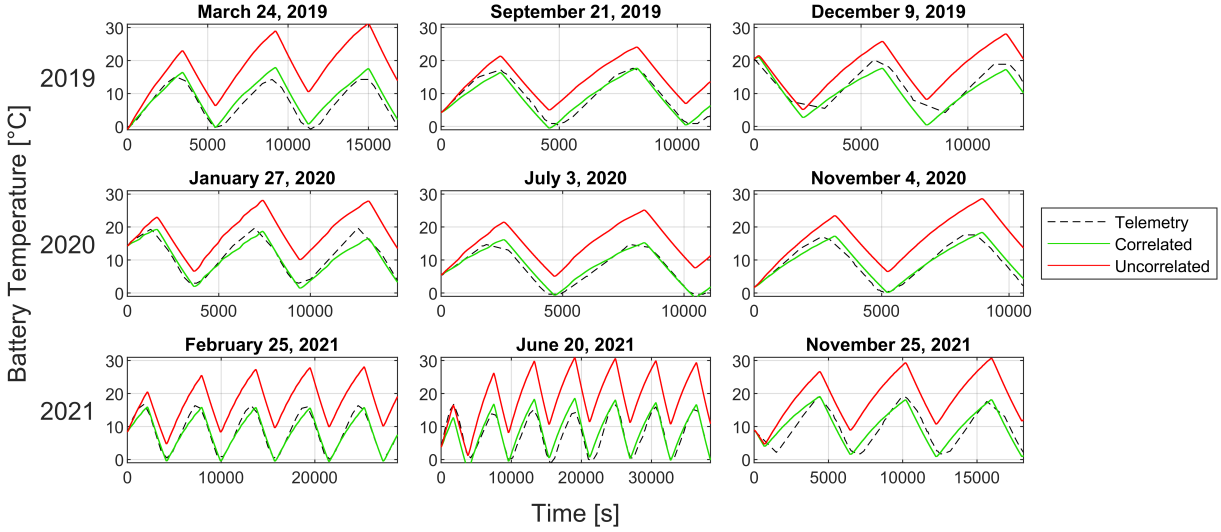

Fig. 5–10: Collection of Different Correlation Results

5.3 Problems Faced

As MOVE-II is suffering from a slightly negative power budget, the satellites CDH transitions to a safemode during most eclipse phases as soon as a certain voltage level of the battery has been fallen below. When the battery charge is restored to a sufficient level, the satellite continues with its normal operation. Unfortunately, the CDH tends to freeze during low temperature events, which triggers EPS watchdog resets [2]. This means that the onboard clock also freezes during this time period and resumes its work after waking up again. Therefore data collected right before this event appears temporarily right next to data recorded after the resuming of normal operation. As a result

the recorded data has no gaps but rather leaps, which means temperature changes can look more drastic than they are in reality or orbit lengths measured by means of the telemetry data received from the satellite seem shorter than they should be. It would be possible to adjust the telemetry data by adding successive temporal offsets, but this would amount to a great effort and would ultimately lead to falsified results, as the comparative data, to which the telemetry data will be adjusted to, arises from the simulation itself. What was done here instead, is to look for data sets that are not visibly corrupted and leave them as they are.

Another problem that was faced, were the high turn rates that MOVE-II is experiencing. As stated before in subsection 3.2.2, an initial angular velocity of $\omega_{b,bi,0} = [0.1\ 0.1\ 0.1]$ 1/s was assumed. Due to the symmetry of the thermal model, the angular velocity should not have a significant influence on the simulated temperatures, as long as the satellite is in motion. The assumed rotation speed $\omega_{b,bi,0}$ is considered high enough for a uniform temperature distribution.

5.4 Comparison to ESATAN® Model

The thermal behaviour of MOVE-II was simulated in an ESATAN-TMS® model prior to launch, in order to achieve an optimal thermal design. This model is composed of 2597 nodes and was verified using steady state TVAC tests. As it turned out these tests were unfortunately not able to provide a good foundation for the transient thermal behavior estimation, as the maximum deviation of the measured battery temperature after launch from its estimations was about 25 °C. Therefore, a correlation of the existing ESATAN-TMS® model was conducted by altering the model's parameters. Thereby, an improvement in the maximum temperature deviation by over 10 K from 25 °C to just below 15 °C was achieved. [12]

A comparison between the uncorrelated and correlated ESATAN-TMS® model by Hannemann [12] and the here correlated Simulink® model is shown in Figure 5–11 for a simulated orbit on February 25 in 2021 (data set 21-08). As a starting point the crossing of the satellite over the Earth's equator (x-y plane in Earth-centered inertial (ECI) frame) in northwards direction was chosen. Both simulations are compared to each other after a settling time of a few orbits, in order to allow for the transient oscillation of the temperature to settle down.

By looking at Figure 5–11, it becomes apparent that the correlation of the simplified Simulink® model (3 nodes) was far more successful than the correlation of the more complex ESATAN-TMS® model (2597 nodes). For comparison: The here displayed simulation of the Simulink® model features a RMSE of 1.36 K, whereas even the correlated ESATAN-TMS® model shows a RMSE of as high as 7.14 K and the uncorrelated model has a RMSE of 8.64 K. This is due to the number of parameters that have to be tuned in a complex model, in order to achieve good results. With less parameters it is far easier to obtain a reasonably good fit with the help of only little orbit data. This was also proven by Rossi and Ivanov with the correlation of a thermal model of the SwissCube CubeSat [10], as their model only consist of 2 nodes: an inner and an

outer sphere. Their correlation yielded a resulting model with a maximum temperature deviation of 3.0 K from the orbit data.

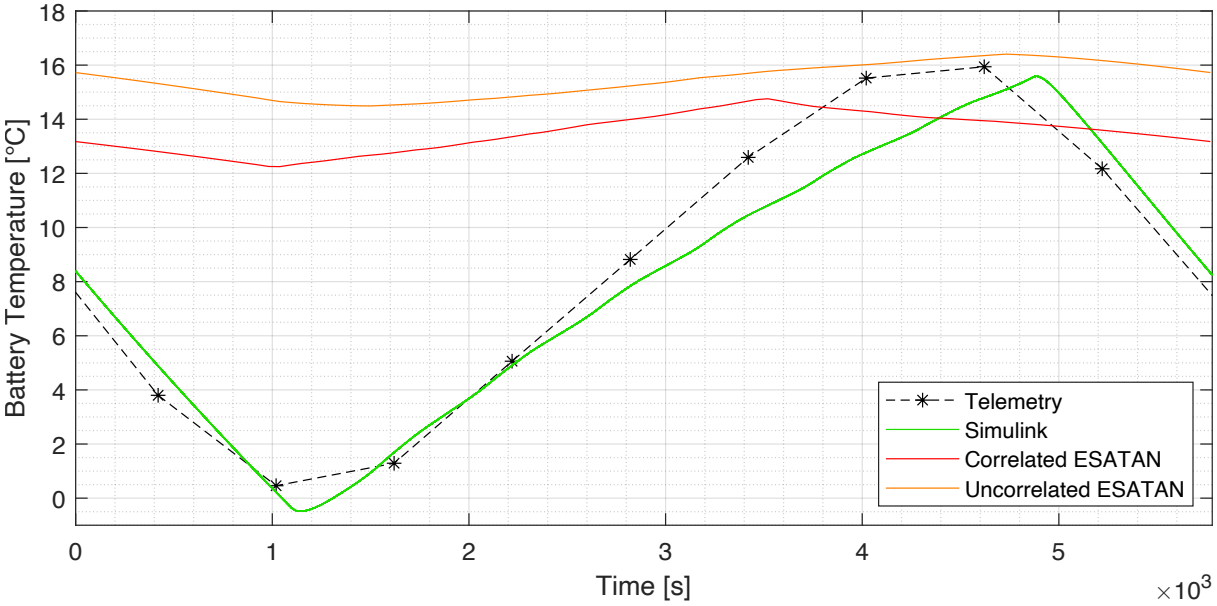

Fig. 5–11: Comparison of Correlated Simulink Model (Simplified) and Both Uncorrelated and Correlated ESATAN Models (Complex)

Furthermore a potential modelation error in the correlated ESATAN-TMS® model can be observed in Figure 5–11. The rise in temperature is significantly shorter than observed in the telemetry data or in the Simulink® model. This is probably due to a highly simplified satellite orbit, used in ESATAN-TMS®, as the orbital plane of the SSO modeled there is parallel to the Earth-Sun vector. This is very similar to a SSO with LTAN $=$ 12 pm, which is incorrect as the LTAN of MOVE-II is equal to 10 pm. Therefore the eclipse time in Hannemann's [12] simulation is too long, which, if corrected, would lead to an even higher temperature deviation of the ESATAN-TMS® model compared to the real satellite.

6 Discussion

In chapter 4 and chapter 5 many findings about the in-orbit data and the correlation of the digital twin were made respectively and will be discussed in the following.

Since MOVE-II is suffering form a low power budget, worsened by the fact that it is not able to reliably stay in sun-point mode, its uptime, defined by the time the satellite did not reboot, is varying greatly with a periodicity of about one year. The maximum values are reached during December and January, as shown in Figure 4–10. This perfectly coincides with the battery temperature, depicted in Figure 4–1, as its maximum values are also recorded during these periods. This correlation can be explained by the direct dependence between temperature and the capacity of the battery [25]. As the SOH of the battery decreases over time and with every cycle [23], the drop in the yearly maxima of uptime are an expected effect, while the maxima and minima of temperature are roughly staying constant. Another evidence for the temperature dependence of the satellite's uptime is the approximated OCV of the battery, which is plotted in Figure 4–6, and which is directly dependent on the amount and intensity of sunlight falling on the satellite. It also shows a spike around January 2020, coinciding with a local maximum in the satellite's uptime.

To account for the observed fluctuations in temperature, two theories have been put forward in subsection 4.1.2, involving the eccentricity of the Earth's orbit and variations in eclipse times of MOVE-II throughout the year. It has been found that the former should have a greater effect on the satellites temperature, as the eclipse times only vary by a small amount for SSOs. However, the actual relationship between these two influences cannot be determined and it cannot be ruled out that there are other factors influencing the temperature of the satellite on a yearly scale, let alone its battery temperature.

Also observed was a rise in the battery's averaged DCIR of 140.4 $\mathrm{m}\Omega$ per year, as shown in Figure 4–3. As the lithium-ion battery of MOVE-II is subject to harsh environmental conditions, such as low temperatures and rapid charging and discharging cycles, caused by the high rotational speed paired with the uneven distribution of solar cells on its surface, the battery's capacity (and its SOH) decrease, as its internal resistance increases [24]. Therefore the here observed increase in DCIR is expected and a sign of the battery's degradation.
Furthermore a dependence of the DCIR on temperature and voltage could be determined individually. As the voltage of the battery is dependent on its temperature, the independently derived empirical Equations 4–6 and 4–8 for the DCIR with respect to temperature and voltage respectively, must be regarded with caution. Due to their cross coupling, the uncertainty of determining the exact SOC, and the lack of evenly distributed measurements on all temperature and voltage ranges, it was not possible to derive an equation for R_{bat} as a function of temperature *and* voltage. The existing model of the battery only features a temperature dependent resistance estimation and only the associated parameters for this dependence were updated, according to Equa-

tion 4–6. A voltage dependent resistance was not modeled, since it would interfere with the dominant influence on the DCIR by the temperature. The accuracy of the data acquisition of the temperature dependent DCIR form orbit data was, moreover, verified by a reversed analysis of the model output data in subsection 4.2.2. Thereby it was confirmed that the used methods were of high precision.

In chapter 5 the thermal simulation model of MOVE-II was correlated with data of over three years. This correlation was conducted by adjusting the optical properties of the satellite, the thermal resistance between the inner and outer node, and the thermal capacitance of these. By far the biggest change in the introduced objective fit measurement (the change in RMSE) was achieved by a modification of the optical properties of the outer shell, through a change of emissivity $\epsilon_{ext,IR}$ and absorptivity $\alpha_{ext,sol}$. The other measures, which were applied to the already modified model with regard to $\epsilon_{ext,IR}$ and $\alpha_{ext,sol}$, had little to no positive effect on the RMSE. Therefore the changes in thermal resistance between the inner and outer node and the change in thermal capacitance of these were discarded. A better optimum could have potentially been found, if a more iterative approach would have been used, where the parameters are altered in different orders and varying quantity. Nonetheless the correlation should be regraded as very successful, since the RMSE could be reduced by a factor of 7 to only 1.36 K on the comparison data set 21-08 (see section 5.2), which is a satisfying result. All this was achieved by reducing the ratio between absorptivity and emissivity ($\alpha_{ext,sol}/\epsilon_{ext,IR}$) from 1.0 to 0.78, which essentially resulted in a better cooling of the simulated satellite. The comparison between the correlated and uncorrelated model can be reviewed in Figure 5–9.
Notably, the correlated α to ϵ ratio for data sets from 2019 (first year after launch) was a little lower at 0.75. This increase during the mission duration could potentially indicate a degradation of the matt white paint, with which side and top panels are coated, after the first year. This, however, is of high uncertainty, as the correlated ratio for 2019 was extracted from only four data sets due to the lack of consistent data during this time frame.
Furthermore the third node, representing the Flappanels, was not touched at all during the correlation process. Since it only has an indirect impact on the battery temperature and the results were already satisfactory, there was no need to adjust the Flappanel parameters.
Also, the battery heater, installed in MOVE-II, was not taken into account. This could potentially lead to false results, especially at low temperatures where the heater is active (activates below 1 °C and deactivates above 6.5 °C), but was not seen as great issue, since the heating power is low at only 0.2 W [4].

The comparison to the previously performed correlation of the by far more complex ESATAN-TMS® model by Hannemann [12] is of special interest (see section 5.4). Due to the complexity of the model and the associated number of parameters, a correlation by hand is orders of magnitude more difficult. This is particularly well illustrated in Figure 5–11, which compares the here correlated temperature model of the battery with the correlated ESATAN-TMS® model.

7 Conclusion and Future Perspectives

As stated before, one of the main problems MOVE-II is facing are the low temperatures, especially during eclipse, which were not, or rather wrongly predicted prior to launch. This miscalculation is a result of an over-complicated thermal model and insufficient TVAC testing [12]. The here performed correlation was, moreover, proven to be by far more successful than the correlation attempt conducted by Hannemann on the complex ESATAN-TMS® model [12]. Therefore, the proposal made here is: Save time and money while designing CubeSats, by avoiding overly complex thermal simulations. Instead invest in extensive TVAC tests, both for steady state and transient case, and a good pre-flight correlation of the thermal model form the test data. This model also does not have to be very complex, as here only three nodes were needed, in order to obtain satisfying results for one subsystem. The thermal correlation conducted on the thermal model of SwissCube's battery even managed to achieve good results with only two nodes [10].

From this it can be drawn that small thermal models, like the one presented here, are a well suited alternative for the simulation of specific subsystems. In case more than one subsystem is to be simulated, an extension of the model is easily feasible. This, however, would make the correlation more difficult again. Another option that has to be considered and should be analyzed in the future is to correlate multiple small models, each for one subsystem of the satellite, with a minimal amount of nodes, by the use of orbit data or data acquired in TVAC tests. This could potentially decrease the correlation effort, as the execution of such correlations can be quickly done. Nevertheless, it should not be forgotten that these simple thermal models only are applicable to small satellites, like CubeSats, in which the thermal propagation is more uniform than in satellites of larger size and where exact thermal simulations on small scales is usually not necessary.

Thermal simulations are not only important for the design process of a satellite, but can also help to gain deeper insights into the operation of a satellite in orbit. Especially in the case of MOVE-II, it is a not inconsiderable effort to obtain consistent and uncorrupted data from the satellite. Therefore, thermal simulations can significantly increase the data density, by extrapolating from the satellite data in a physically sound manner. This can be particularly useful in terms of fault analysis and mission planning.

In order to increase the accuracy of the here presented thermal model, several improvements could be made: Besides the implementation of the battery heater, further correlations could be conducted on the outer shell and the Flappanels. By doing so, it would be possible to extract exact temperature readings from the Flappanels, which was not possible before, due to the lack of temperature sensors on these. Regarding the battery model of MOVE-II, a voltage and temperature dependent implementation of the internal battery resistance could be added, in contrast to the currently used resistance calculation, which depends only on temperature. In addition, an advanced analysis could be conducted on the current SOH of the battery, which would greatly

increase the accuracy of the whole simulation. As stated before, the correlated thermal model is part of a large digital twin, which not only includes thermals, but also the ADCS and electrical system of the satellite. From the in-orbit data it should be possible to also correlate other subsystems to a high level of accuracy. This could involve, for example, an analysis of the efficiency of the ADCS actuators and an implementation of the findings into the Simulink® model.

In addition, it is always useful to keep data analysis and model correlation in mind when developing the satellite, as this can provide deeper insights into the state of the satellite later, during operation. In the case of MOVE-II, this would have meant incorporating battery resistance measurement devices directly onboard to obtain more accurate readings, and possibly the addition of integrated logic capable of determining battery SOC, through the use of the *coulomb counting* technique or equivalent methods.

Concluding this data analysis and digital twin correlation, it hopefully became apparent that the solution to a complex problem can often be very simple. This should be taken as an inspiration, as the world of satellites is becoming more and more diverse and it should always be checked, if important resources could potentially be used in a smarter and more profitable way.

Bibliography

[1] California Polytechnic State University, “CubeSat Design Specification Rev. 14.1,” San Luis Obispo, CA, 2022.

[2] S. Rückerl, D. Messmann, N. Appel, J. Kiesbye, F. Schummer, M. Faehling, L. Krempel, T. Kale, A. Lill, G. J. Reina Kiperman, P. Schnierle, S. Würl, M. Langer, and M. Lülf, “First Flight Results of the MOVE-II Satellite,” no. SSC19-WKI-07. Logan, Utah: 33rd Annual Small Satellite Conference, 08 2019.

[3] M. Langer, F. Schummer, N. Appel, T. Grübler, K. Janzer, J. Kiesbye, L. Krempel, A. Lill, D. Messmann, S. Rückerl, and M. Weisgerber, “MOVE-II THE MUNICH ORBITAL VERIFICATION EXPERIMENT II,” 12 2017.

[4] M. Langer, F. Schummer, S. Rückerl, D. Vogel, A. Lill, R. Amann, T. Kale, K. Janzer, L. Krempel, J. Kiesbye, and P. Lu, “System documentation move-ii,” Technical University of Munich, Chair of Astronautics, Tech. Rep., 2019.

[5] L. Volk, R. Borrek, N. Zischka, J. Koch, I. Sharma, M. Nardini, L. Holl, S. Gruber, F. Schummer, J. Kiesbye, and D. Messmann, “New Results and Lessons Learned from the MOVE-II and MOVE-IIb CubeSats,” no. SSC22-WKP2-02. Logan, Utah: 36th Annual Small Satellite Conference, 08 2022.

[6] S. Gruber, “Status Analysis and Investigations of a semi-functional Satellite in Space,” 2020, semester thesis, Technical University of Munich Chair of Astronautics.

[7] J. Meseguer, I. Pérez-Grande, and A. Sanz-Andrés, “2 - space environment,” in *Spacecraft Thermal Control*, J. Meseguer, I. Pérez-Grande, and A. Sanz-Andrés, Eds. Woodhead Publishing, 2012, pp. 15–38. [Online]. Available: https://www.sciencedirect.com/science/article/pii/B9781845699963500022

[8] IEC, *Akkumulatoren und Batterien mit alkalischen oder anderen nichtsäurehaltigen Elektrolyten – Lithium-Akkumulatoren und -batterien für tragbare Geräte*. Beuth Verlag, Berlin, 2012.

[9] M. Á. C. Perpiñán, A. C. Perpi *et al.*, “The modelling of the thermal subsystem in spacecraft real-time simulators,” 1994.

[10] S. Rossi and A. Ivanov, “Thermal model for cubesat: A simple and easy model from the swisscube’s thermal flight data,” 09 2013.

[11] S.-J. Kang and H.-U. Oh, “On-orbit thermal design and validation of 1 u standardized cubesat of step cube lab,” *International Journal of Aerospace Engineering*, vol. 2016, pp. 1–17, 06 2016.

[12] L. Hannemann, “Analysis and Correlation of the Thermal Model for the MOVE-II CubeSat,” 2019.

[13] MATLAB, *version 9.10.0 (R2021a)*. Natick, Massachusetts: The MathWorks Inc., 2010.

[14] J. Kiesbye, D. Messmann, M. Preisinger, G. Reina, D. Nagy, F. Schummer, M. Mostad, T. Kale, and M. Langer, “Hardware-in-the-loop and software-in-the-loop testing of the move-ii cubesat,” *Aerospace*, vol. 6, no. 12, 2019. [Online]. Available: https://www.mdpi.com/2226-4310/6/12/130

[15] I. Pérez-Grande, A. Sanz-Andrés, C. Guerra, and G. Alonso, “Analytical study of the thermal behaviour and stability of a small satellite,” *Applied Thermal Engineering*, vol. 29, no. 11, pp. 2567–2573, 2009. [Online]. Available: https://www.sciencedirect.com/science/article/pii/S1359431108005036

[16] U. Walter, *Orbit Geometry and Determination*. Cham: Springer International Publishing, 2018, pp. 677–697. [Online]. Available: https://doi.org/10.1007/978-3-319-74373-8_14

[17] G. Kirchhoff, “Über das Verhältniss zwischen dem Emissionsvermögen und dem Absorptionsvermögen der Körper für Wärme und Licht,” *Annalen der Physik*, vol. 185, no. 2, pp. 275–301, 1860. [Online]. Available: https://onlinelibrary.wiley.com/doi/abs/10.1002/andp.18601850205

[18] G. Datseris and B. Stevens, “Earth’s albedo and its symmetry,” *AGU Advances*, vol. 2, no. 3, p. e2021AV000440, 2021, e2021AV000440 2021AV000440. [Online]. Available: https://agupubs.onlinelibrary.wiley.com/doi/abs/10.1029/2021AV000440

[19] J. L. Simon, P. Bretagnon, J. Chapront, M. Chapront-Touze, G. Francou, and J. Laskar, “Numerical expressions for precession formulae and mean elements for the Moon and the planets.” *Astronomy and Astrophysics*, vol. 282, p. 663, Feb. 1994.

[20] F. Espenak. (2021) Earth at perihelion and aphelion: 2001 to 2100. [Online]. Available: http://www.astropixels.com/ephemeris/perap2001.html

[21] G. Kopp and J. L. Lean, “A new, lower value of total solar irradiance: Evidence and climate significance,” *Geophysical Research Letters*, vol. 38, no. 1, 2011. [Online]. Available: https://agupubs.onlinelibrary.wiley.com/doi/abs/10.1029/2010GL045777

[22] D. A. Vallado, *Fundamentals of astrodynamics and applications*, 3rd ed., ser. Space technology library. Hawthorne, Calif.: Microcosm Press [u.a.], 2007.

[23] L. Yao, S. Xu, A. Tang, F. Zhou, J. Hou, Y. Xiao, and Z. Fu, “A review of lithium-ion battery state of health estimation and prediction methods,” *World Electric Vehicle Journal*, vol. 12, no. 3, 2021. [Online]. Available: https://www.mdpi.com/2032-6653/12/3/113

[24] M. Fleischhammer, T. Waldmann, G. Bisle, B.-I. Hogg, and M. Wohlfahrt-Mehrens, “Interaction of cyclic ageing at high-rate and low temperatures and safety in lithium-ion batteries,” *Journal of Power Sources*, vol. 274, pp. 432–439, 2015. [Online]. Available: https://www.sciencedirect.com/science/article/pii/S037877531401489X

[25] S. Ma, M. Jiang, P. Tao, C. Song, J. Wu, J. Wang, T. Deng, and W. Shang, “Temperature effect and thermal impact in lithium-ion batteries: A review,” *Progress in Natural Science: Materials International*, vol. 28, no. 6, pp. 653–666, 2018.

[26] Würth Elektronik. Lötstopplack. [Online]. Available: https://www.wedirekt.de/de/web/technologie/leiterplatten-technologie/spezifikation/loetstopplack.fs-227741.html

A Appendix

A.1 Parameters for Thermal Simulink Model

The following two Tables A–1 and A–2 present all initial and tuned parameters of the thermal model, respectively. In Table A–2, the altered parameters and changed values were additionally highlighted.

Tab. A–1: Initial Thermal Parameters used in Simulink Model

Subsystem	Name	Symbol	Value	Unit
Earth	Albedo	a	0.3	-
	Emissivity	$\epsilon_{earth,IR}$	0.9	-
	Temperature	T_{earth}	288.15	K
Outer Sphere	Diameter Exterior	$d_{ext,outer}$	0.11	m
	Diameter Interior	$d_{ext,inner}$	0.107	m
	Emissivity	$\epsilon_{ext,IR}$	0.7	-
	Absorptivity	$\alpha_{ext,sol}$	0.7	-
	Specific Thermal Capacity	$c_{p,ext}$	687	J/(kg K)
	Density	ρ_{ext}	3666.7	kg/m^3
	View Factor Planet	$F_{ext\rightarrow earth}$	0.5	-
	View Factor Albedo	$F_{ext\rightarrow albedo}$	0.5	-
Inner Sphere	Diameter	d_{int}	0.09	m
	Emissivity	$\epsilon_{int,IR}$	0.7	-
	Specific Thermal Capacity	$c_{p,int}$	994.89	J/(kg K)
	Density	ρ_{int}	2297.4	kg/m^3
	Conductive Surface	$A_{ext\rightarrow int,c}$	8×10^{-4}	m^2
	Conductivity Aluminium	λ_{al}	237	W/(m K)
	Solder Mask Thickness	h_{mask}	5×10^{-5}	m
	Conductivity Solder Mask	λ_{mask}	0.2	W/(m K)
Flappanels	Radiating Area	A_{fp}	0.064	m^2
	Volume	V_{fp}	4×10^{-5}	m^3
	Emissivity	$\epsilon_{fp,IR}$	0.7	-
	Absorptivity	$\alpha_{fp,sol}$	0.7	-
	Specific Thermal Capacity	$c_{p,fp}$	518.5	J/(kg K)
	Density	ρ_{fp}	3410	kg/m^3
	Length Hinge	l_h	0.02	m
	Conductivity Hinge	λ_h	23.5	W/(m K)
	Cross Section Area Hinge	A_h	2×10^{-5}	m^2
	View Factor Sun	$F_{sun\rightarrow fp}$	0.4	-
	View Factor Planet	$F_{earth\rightarrow fp}$	0.4	-

Tab. A–2: Correlated Thermal Parameters used in Simulink Model

Subsystem	Name	Symbol	Value	Unit
Earth	Albedo	a	0.3	-
	Emissivity	$\epsilon_{earth,IR}$	0.9	-
	Temperature	T_{earth}	288.15	K
Outer Sphere	Diameter Exterior	$d_{ext,outer}$	0.11	m
	Diameter Interior	$d_{ext,inner}$	0.107	m
	Emissivity	$\epsilon_{ext,IR}$	**0.79**	-
	Absorptivity	$\alpha_{ext,sol}$	**0.62**	-
	Specific Thermal Capacity	$c_{p,ext}$	687	J/(kg K)
	Density	ρ_{ext}	3666.7	kg/m^3
	View Factor Planet	$F_{ext\rightarrow earth}$	0.5	-
	View Factor Albedo	$F_{ext\rightarrow albedo}$	0.5	-
Inner Sphere	Diameter	d_{int}	0.09	m
	Emissivity	$\epsilon_{int,IR}$	0.7	-
	Specific Thermal Capacity	$c_{p,int}$	994.89	J/(kg K)
	Density	ρ_{int}	2297.4	kg/m^3
	Conductive Surface	$A_{ext\rightarrow int,c}$	8×10^{-4}	m^2
	Conductivity Aluminium	λ_{al}	237	W/(m K)
	Solder Mask Thickness	h_{mask}	5×10^{-5}	m
	Conductivity Solder Mask	λ_{mask}	0.2	W/(m K)
Flappanels	Radiating Area	A_{fp}	0.064	m^2
	Volume	V_{fp}	4×10^{-5}	m^3
	Emissivity	$\epsilon_{fp,IR}$	0.7	-
	Absorptivity	$\alpha_{fp,sol}$	0.7	-
	Specific Thermal Capacity	$c_{p,fp}$	518.5	J/(kg K)
	Density	ρ_{fp}	3410	kg/m^3
	Length Hinge	l_h	0.02	m
	Conductivity Hinge	λ_h	23.5	W/(m K)
	Cross Section Area Hinge	A_h	2×10^{-5}	m^2
	View Factor Sun	$F_{sun\rightarrow fp}$	0.4	-
	View Factor Planet	$F_{earth\rightarrow fp}$	0.4	-

A.2 Data Sets for Simulation Verification

Table A–3 lists all data sets that were used for the correlation of the thermal simulation model, together with stat and end date, the total duration and the offset applied.

Tab. A–3: Data Sets for Simulation Verification

Name	Date Start (UTC)	Date End (UTC)	Duration	Offset [s]
19-01	2019-03-24 01:59:27	2019-03-24 06:39:31	04:40:04	-600
19-02	2019-08-27 09:13:31	2019-08-27 14:13:35	05:00:04	+300
19-03	2019-09-21 13:24:24	2019-09-21 16:34:27	03:10:03	-2374
19-04	2019-12-09 10:54:18	2019-12-09 14:24:21	03:30:03	+942
20-01	2020-01-27 22:37:20	2020-01-28 02:43:23	04:06:03	+2313
20-02	2020-01-30 22:30:52	2020-01-31 02:36:57	04:06:05	-1888
20-03	2020-05-27 20:45:48	2020-05-27 23:43:51	02:58:03	-303
20-04	2020-07-03 08:12:08	2020-07-03 11:16:54	03:04:46	-500
20-05	2020-07-17 02:10:45	2020-07-17 05:09:48	02:59:03	+2693
20-06	2020-08-03 01:31:31	2020-08-03 04:17:33	02:46:02	-1195
20-07	2020-10-14 07:59:43	2020-10-14 10:25:46	02:26:03	+250
20-08	2020-10-15 08:11:02	2020-10-15 10:45:04	02:34:02	-320
20-09	2020-10-31 07:16:48	2020-10-31 10:16:50	03:00:02	+397
20-10	2020-11-04 07:56:48	2020-11-04 10:52:51	02:56:03	-830
20-11	2020-11-13 17:14:41	2020-11-13 20:10:43	02:56:02	-2100
20-12	2020-12-21 23:12:18	2020-12-22 02:10:20	02:58:02	-243
20-13	2020-12-23 07:23:06	2020-12-23 10:29:08	03:06:02	-550
21-01	2021-01-03 07:04:35	2021-01-03 11:11:39	04:07:04	-600
21-02	2021-01-07 03:21:19	2021-01-07 07:23:22	04:02:03	+2600
21-03	2021-01-26 07:00:45	2021-01-26 11:29:53	04:29:08	-600
21-04	2021-01-27 05:25:28	2021-01-27 08:53:30	03:28:02	-2013
21-05	2021-01-29 02:10:58	2021-01-29 07:05:02	04:54:04	-1396
21-06	2021-02-07 08:00:55	2021-02-07 11:25:03	03:24:08	-600
21-07	2021-02-25 03:18:00	2021-02-25 05:48:02	02:30:02	-1750
21-08	2021-02-25 15:56:29	2021-02-25 23:56:35	08:00:06	0
21-09	2021-04-10 00:39:56	2021-04-10 09:01:02	08:21:06	+1160
21-10	2021-05-15 14:48:30	2021-05-15 20:38:34	05:50:04	+2540
21-11	2021-05-26 17:41:25	2021-05-26 22:35:29	04:54:04	-750
21-12	2021-06-20 10:55:57	2021-06-20 21:36:05	10:40:08	-370
21-13	2021-10-09 20:21:50	2021-10-10 02:15:54	05:54:04	+1692
21-14	2021-11-18 05:46:16	2021-11-18 08:44:19	02:58:03	+2550
21-15	2021-11-25 18:03:04	2021-11-25 23:05:08	05:02:04	-1064
21-16	2021-12-09 11:15:12	2021-12-09 23:35:21	12:20:09	-550

A.3 Simulation Results

The here presented tables show the individual simulation results, that average to the results, that were shown in section 5.1. The following subsections also show the same structure. Some of the tables are duplicates, but are shown for completeness and for the sake of a better overview.

A.3.1 Emissivity and Absorptivity Adaption of the Outer Sphere

Tab. A–4: Simulation Results of 2019 Data Sets with $\epsilon_{ext,IR} = 0.77$ and $\alpha_{ext,sol} = 0.58$

Data Set	$\epsilon_{ext,IR}$	$\alpha_{ext,sol}$	RMSE [K]	Absolute Difference in Trend [10^{-6} $\frac{K}{s}$]
19-01	0.77	0.58	1.0002	58.2738
19-02			3.4439	204.8387
19-03			1.5368	324.4657
19-04			2.7874	168.8745
Average:			2.1921	189.1132

Tab. A–5: Simulation Results of 2019 Data Sets with $\epsilon_{ext,IR} = 0.79$ and $\alpha_{ext,sol} = 0.60$

Data Set	$\epsilon_{ext,IR}$	$\alpha_{ext,sol}$	RMSE [K]	Absolute Difference in Trend [10^{-6} $\frac{K}{s}$]
19-01	0.79	0.60	1.8120	126.1159
19-02			3.3149	180.3731
19-03			1.4484	266.3126
19-04			2.7928	133.5107
Average:			2.342	176.5781

Tab. A–6: Simulation Results of 2019 Data Sets with $\epsilon_{ext,IR} = 0.79$ and $\alpha_{ext,sol} = 0.62$

Data Set	$\epsilon_{ext,IR}$	$\alpha_{ext,sol}$	RMSE [K]	Absolute Difference in Trend [10^{-6} $\frac{K}{s}$]
19-01	0.79	0.62	1.4089	76.9689
19-02			3.7321	244.3938
19-03			1.5856	341.7214
19-04			2.3724	96.1159
Average:			2.2748	189.8000

Tab. A–7: Simulation Results of 2020 Data Sets with $\epsilon_{ext,IR} = 0.77$ and $\alpha_{ext,sol} = 0.58$

Data Set	$\epsilon_{ext,IR}$	$\alpha_{ext,sol}$	RMSE [K]	Absolute Difference in Trend [10^{-6} $\frac{K}{s}$]
20-01			1.8595	9.3319
20-02			1.6561	276.8869
20-03			1.0145	547.3274
20-04			0.9044	3.9424
20-05			1.2355	360.8066
20-06			1.8528	36.9420
20-07	0.77	0.58	1.1403	131.5193
20-08			1.8150	337.4180
20-09			1.4101	472.6180
20-10			1.5570	87.2145
20-11			2.7462	178.1459
20-12			5.0385	75.8220
20-13			3.6734	280.7450
Average:			1.9926	215.2861

Tab. A–8: Simulation Results of 2020 Data Sets with $\epsilon_{ext,IR} = 0.79$ and $\alpha_{ext,sol} = 0.60$

Data Set	$\epsilon_{ext,IR}$	$\alpha_{ext,sol}$	RMSE [K]	Absolute Difference in Trend [10^{-6} $\frac{K}{s}$]
20-01			2.1097	42.5245
20-02			1.8751	242.7717
20-03			1.0557	525.9167
20-04			0.9385	8.5199
20-05			2.9140	67.3700
20-06			1.7829	225.5538
20-07	0.79	0.60	1.0851	160.6974
20-08			1.8876	303.1244
20-09			1.2186	448.2116
20-10			1.4316	75.4544
20-11			2.8241	182.6375
20-12			5.1518	74.9072
20-13			3.7695	278.7075
Average:			2.1572	202.7997

Tab. A–9: Simulation Results of 2020 Data Sets with $\epsilon_{ext,IR} = 0.79$ and $\alpha_{ext,sol} = 0.62$

Data Set	$\epsilon_{ext,IR}$	$\alpha_{ext,sol}$	RMSE [K]	Absolute Difference in Trend [10^{-6} $\frac{K}{s}$]
20-01	0.79	0.62	1.6142	33.0966
20-02			1.4345	320.8320
20-03			1.3368	575.7986
20-04			1.0962	17.0483
20-05			1.0062	385.0629
20-06			1.6812	6.1836
20-07			1.1865	77.2572
20-08			1.9750	382.2353
20-09			1.5897	496.8320
20-10			1.6938	117.3906
20-11			2.4711	206.1646
20-12			4.7162	45.7960
20-13			3.2886	304.8278
Average:			1.9300	228.3481

Tab. A–10: Simulation Results of 2021 Data Sets with $\epsilon_{ext,IR} = 0.77$ and $\alpha_{ext,sol} = 0.58$

Data Set	$\epsilon_{ext,IR}$	$\alpha_{ext,sol}$	RMSE [K]	Absolute Difference in Trend [10^{-6} $\frac{K}{s}$]
21-01	0.77	0.58	2.9854	365.2230
21-02			1.9610	183.7520
21-03			2.8382	190.0612
21-04			2.8033	326.3352
21-05			1.9261	79.9824
21-06			2.1789	83.4485
21-07			2.0705	314.4416
21-08			1.3342	7.9283
21-09			1.6844	50.6980
21-10			2.2771	52.4850
21-11			2.2703	351.8394
21-12			2.4543	106.7938
21-13			1.9375	9.7622
21-14			3.4120	66.5045
21-15			2.3362	89.4080
21-16			2.4329	77.7029
Average:			2.3064	147.2729

Tab. A–11: Simulation Results of 2021 Data Sets with $\epsilon_{ext,IR} = 0.79$ and $\alpha_{ext,sol} = 0.60$

Data Set	$\epsilon_{ext,IR}$	$\alpha_{ext,sol}$	RMSE [K]	Absolute Difference in Trend [10^{-6} $\frac{K}{s}$]
21-01	0.79	0.60	2.9050	317.9660
21-02			2.2523	320.1735
21-03			3.0762	213.5167
21-04			2.9790	367.3101
21-05			2.2454	61.0258
21-06			2.4862	25.1949
21-07			2.1759	364.9935
21-08			1.3912	31.2972
21-09			1.5557	18.1569
21-10			1.9552	8.3035
21-11			2.2225	343.4534
21-12			1.8808	71.1528
21-13			1.7907	36.3818
21-14			3.4940	69.8900
21-15			2.3696	112.7526
21-16			2.3282	66.4036
Average:			2.3193	151.7483

Tab. A–12: Simulation Results of 2021 Data Sets with $\epsilon_{ext,IR} = 0.79$ and $\alpha_{ext,sol} = 0.62$

Data Set	$\epsilon_{ext,IR}$	$\alpha_{ext,sol}$	RMSE [K]	Absolute Difference in Trend [10^{-6} $\frac{K}{s}$]
21-01	0.79	0.62	2.5743	323.2401
21-02			1.6987	138.9723
21-03			2.3784	163.8275
21-04			2.7600	284.5046
21-05			1.5604	114.8174
21-06			1.8048	103.5798
21-07			1.6074	262.8770
21-08			1.2528	21.7759
21-09			1.5168	30.3738
21-10			2.7595	64.0226
21-11			2.6006	392.7097
21-12			2.8544	114.5079
21-13			2.2291	2.1698
21-14			3.2038	92.8014
21-15			2.3850	111.9047
21-16			2.1661	80.8861
Average:			2.2095	143.9357

A.3.2 Thermal Resistance Adaption Between Inner and Outer Sphere

Here, simulations were conducted with variation in the width of the solder mask, which is a main factor in conductive heat transport from the external to the internal node. For parameter sets from 2019 (19-xx) $\epsilon_{ext,IR} = 0.77$ and $\alpha_{ext,sol} = 0.58$ were chosen, whereas for younger parameter sets from 2020 and 2021 (20-xx and 21-xx) $\epsilon_{ext,IR} = 0.79$ and $\alpha_{ext,sol} = 0.62$ was identified as the optimal choice (see subsection 5.1.1). The simulation results presented here are based on these parameters.

Tab. A–13: Simulation Results of 2019 Data Sets with $\lambda_{mask} = 0.2$ W/(m K)

Data Set	λ_{mask}	RMSE [K]	Absolute Difference in Trend [10^{-6} $\frac{K}{s}$]
19-01	0.2	1.0002	58.2738
19-02		3.4439	204.8387
19-03		1.5368	324.4657
19-04		2.7874	168.8745
Average:		2.1921	189.1132

Tab. A–14: Simulation Results of 2019 Data Sets with $\lambda_{mask} = 0.3$ W/(m K)

Data Set	λ_{mask}	RMSE [K]	Absolute Difference in Trend [10^{-6} $\frac{K}{s}$]
19-01	0.3	0.8400	37.6697
19-02		3.2680	201.6532
19-03		1.5482	296.1515
19-04		3.0256	171.3448
Average:		2.1705	176.7047

Tab. A–15: Simulation Results of 2020 Data Sets with $\lambda_{mask} = 0.2$ W/(m K)

Data Set	λ_{mask}	RMSE [K]	Absolute Difference in Trend [10^{-6} $\frac{K}{s}$]
20-01	0.2	1.6142	33.0966
20-02		1.4345	320.8320
20-03		1.3368	575.7986
20-04		1.0962	17.0483
20-05		1.0062	385.0629
20-06		1.6812	6.1836
20-07		1.1865	77.2572
20-08		1.9750	382.2353
20-09		1.5897	496.8320
20-10		1.6938	117.3906
20-11		2.4711	206.1646
20-12		4.7162	45.7960
20-13		3.2886	304.8278
Average:		1.9300	228.3481

Tab. A–16: Simulation Results of 2020 Data Sets with $\lambda_{mask} = 0.3$ W/(m K)

Data Set	λ_{mask}	RMSE [K]	Absolute Difference in Trend [10^{-6} $\frac{K}{s}$]
20-01	0.3	1.7539	20.3519
20-02		1.6601	307.2663
20-03		1.3605	543.9809
20-04		0.9072	13.4618
20-05		1.0620	355.1371
20-06		1.6939	22.5642
20-07		1.1827	100.1644
20-08		2.0517	356.8601
20-09		1.3675	463.7400
20-10		1.5105	86.4004
20-11		2.6588	174.1256
20-12		4.9419	77.6336
20-13		3.5009	274.0805
Average:		1.9732	215.0590

Tab. A–17: Simulation Results of 2021 Data Sets with $\lambda_{mask} = 0.2$ W/(m K)

Data Set	λ_{mask}	RMSE [K]	Absolute Difference in Trend [10^{-6} $\frac{K}{s}$]
21-01	0.2	2.5743	323.2401
21-02		1.6987	138.9723
21-03		2.3784	163.8275
21-04		2.7600	284.5046
21-05		1.5604	114.8174
21-06		1.8048	103.5798
21-07		1.6074	262.8770
21-08		1.2528	21.7759
21-09		1.5168	30.3738
21-10		2.7595	64.0226
21-11		2.6006	392.7097
21-12		2.8544	114.5079
21-13		2.2291	2.1698
21-14		3.2038	92.8014
21-15		2.3850	111.9047
21-16		2.1661	80.8861
Average:		2.2095	143.9357

Tab. A–18: Simulation Results of 2021 Data Sets with $\lambda_{mask} = 0.3$ W/(m K)

Data Set	λ_{mask} [$\frac{\mathrm{W}}{\mathrm{m\,K}}$]	RMSE [K]	Absolute Difference in Trend [10^{-6} $\frac{\mathrm{K}}{\mathrm{s}}$]
21-01	0.3	2.8214	336.3790
21-02		1.9272	149.4247
21-03		2.5687	181.8531
21-04		2.8584	306.7881
21-05		1.7133	102.5972
21-06		1.9843	77.5024
21-07		1.6958	285.0229
21-08		1.1610	14.9766
21-09		1.6191	35.2898
21-10		2.5253	50.4938
21-11		2.3839	386.1580
21-12		2.6712	108.7651
21-13		2.1595	11.0300
21-14		3.3965	61.1139
21-15		2.4605	96.9022
21-16		2.2526	77.2419
Average:		2.2624	142.5961

A.3.3 Thermal Capacitance Adaption

This section contains simulation results from the variation of $c_{p,int}$ on all datasets. Simulations presented here are still based on the optimized parameter set (see Table A–2).

Tab. A–19: Simulation Results of 2019 Data Sets with $c_{p,int} = 894.89$ J/(kg K)

Data Set	$c_{p,int}$ [$\frac{\mathrm{J}}{\mathrm{kg\,K}}$]	RMSE [K]	Absolute Difference in Trend [10^{-6} $\frac{\mathrm{K}}{\mathrm{s}}$]
19-01	894.89	1.0869	20.8954
19-02		3.4248	245.6622
19-03		1.4848	268.2022
19-04		2.8150	99.1569
Average:		2.2029	158.4792

Tab. A–20: Simulation Results of 2019 Data Sets with $c_{p,int} = 994.89$ J/(kg K)

Data Set	$c_{p,int}$ [$\frac{\mathrm{J}}{\mathrm{kg\,K}}$]	RMSE [K]	Absolute Difference in Trend [10^{-6} $\frac{\mathrm{K}}{\mathrm{s}}$]
19-01	994.89	1.0002	58.2738
19-02		3.4439	204.8387
19-03		1.5368	324.4657
19-04		2.7874	168.8745
Average:		2.1921	189.1132

Tab. A–21: Simulation Results of 2020 Data Sets with $c_{p,int} = 894.89\,\mathrm{J/(kg\,K)}$

Data Set	$c_{p,int}$ [$\frac{\mathrm{J}}{\mathrm{kg\,K}}$]	RMSE [K]	Absolute Difference in Trend [10^{-6} $\frac{\mathrm{K}}{\mathrm{s}}$]
20-01	894.89	1.8077	44.2618
20-02		1.7653	333.5219
20-03		1.9129	539.3586
20-04		1.0637	39.5447
20-05		0.9637	338.9339
20-06		1.6921	20.1821
20-07		1.3090	57.8667
20-08		2.3481	383.6939
20-09		1.5149	449.1514
20-10		1.7242	81.9668
20-11		2.5537	165.3406
20-12		4.8611	93.4767
20-13		3.3538	246.5595
Average:		2.0670	214.9122

Tab. A–22: Simulation Results of 2020 Data Sets with $c_{p,int} = 994.89\,\mathrm{J/(kg\,K)}$

Data Set	$c_{p,int}$ [$\frac{\mathrm{J}}{\mathrm{kg\,K}}$]	RMSE [K]	Absolute Difference in Trend [10^{-6} $\frac{\mathrm{K}}{\mathrm{s}}$]
20-01	994.89	1.6142	33.0966
20-02		1.4345	320.8320
20-03		1.3368	575.7986
20-04		1.0962	17.0483
20-05		1.0062	385.0629
20-06		1.6812	6.1836
20-07		1.1865	77.2572
20-08		1.9750	382.2353
20-09		1.5897	496.8320
20-10		1.6938	117.3906
20-11		2.4711	206.1646
20-12		4.7162	45.7960
20-13		3.2886	304.8278
Average:		1.9300	228.3481

Tab. A–23: Simulation Results of 2021 Data Sets with $c_{p,int} = 894.89\,\mathrm{J/(kg\,K)}$

Data Set	$c_{p,int}$ [$\frac{\mathrm{J}}{\mathrm{kg\,K}}$]	RMSE [K]	Absolute Difference in Trend [$10^{-6}\,\frac{\mathrm{K}}{\mathrm{s}}$]
21-01	894.89	2.7204	312.1251
21-02		2.0166	109.9811
21-03		2.3396	184.9458
21-04		2.9529	299.5027
21-05		1.5802	117.4465
21-06		1.8284	44.6715
21-07		1.3018	279.4598
21-08		1.1492	15.6237
21-09		1.6105	23.3022
21-10		2.9921	36.9457
21-11		2.7243	424.1456
21-12		2.9169	106.3184
21-13		2.4533	21.2362
21-14		3.3681	47.4802
21-15		2.6127	99.0538
21-16		2.0771	77.3144
Average:		2.2902	137.4720

Tab. A–24: Simulation Results of 2021 Data Sets with $c_{p,int} = 994.89\,\mathrm{J/(kg\,K)}$

Data Set	$c_{p,int}$ [$\frac{\mathrm{J}}{\mathrm{kg\,K}}$]	RMSE [K]	Absolute Difference in Trend [10^{-6} $\frac{\mathrm{K}}{\mathrm{s}}$]
21-01	994.89	2.5743	323.2401
21-02		1.6987	138.9723
21-03		2.3784	163.8275
21-04		2.7600	284.5046
21-05		1.5604	114.8174
21-06		1.8048	103.5798
21-07		1.6074	262.8770
21-08		1.2528	21.7759
21-09		1.5168	30.3738
21-10		2.7595	64.0226
21-11		2.6006	392.7097
21-12		2.8544	114.5079
21-13		2.2291	2.1698
21-14		3.2038	92.8014
21-15		2.3850	111.9047
21-16		2.1661	80.8861
Average:		2.2095	143.9357

A.4 Verification Model for Internal Battery Resistance Calculations

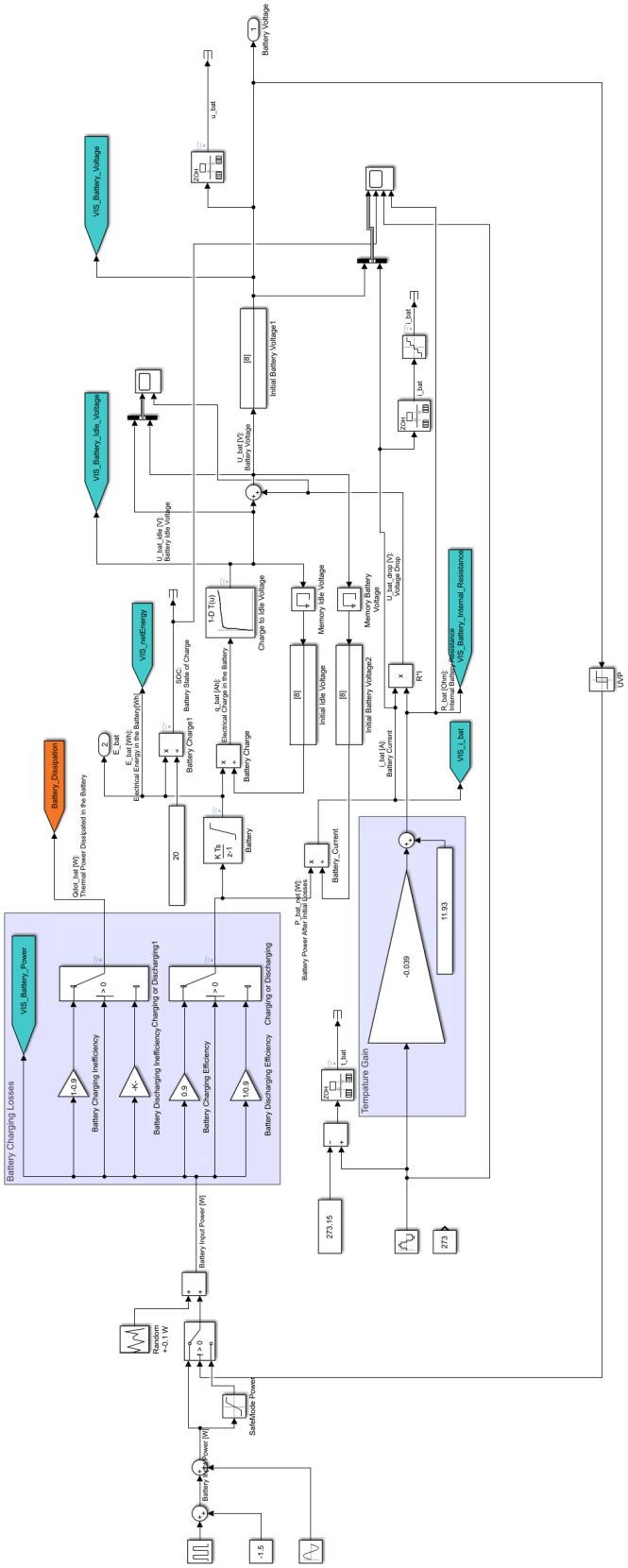

Fig. A–1: Battery Verification Model in Simulink

A.5 Source Code

Link to the Git repository of the simulation model and all scripts developed for this paper:
`https://gitlab.lrz.de/move/design/move_hil/-/tree/orbitdata_correlation`